Icarus 267 (2016) 106–134

Contents lists available at ScienceDirect

Icarus

journal homepage: www.journals.elsevier.com/icarus

Simulating Titan's methane cycle with the TitanWRF General Circulation Model

Claire E. Newman *, Mark I. Richardson, Yuan Lian, Christopher Lee

Aeolis Research, Suite 205, 600 North Rosemead Boulevard, Pasadena, CA 91107, USA

ARTICLE INFO

Article history:
Received 30 August 2013
Revised 13 October 2015
Accepted 14 November 2015
Available online 18 December 2015

Keywords:
Titan
Titan, atmosphere
Atmospheres, dynamics
Atmospheres, structure
Meteorology

ABSTRACT

Observations provide increasing evidence of a methane hydrological cycle on Titan. Earth-based and Cassini-based monitoring has produced data on the seasonal variation in cloud activity and location, with clouds being observed at increasingly low latitudes as Titan moved out of southern summer. Lakes are observed at high latitudes, with far larger lakes and greater areal coverage in the northern hemisphere, where some shorelines extend down as far as 50°N. Rainfall at some point in the past is suggested by the pattern of flow features on the surface at the Huygens landing site, while recent rainfall is suggested by surface change. As with the water cycle on Earth, the methane cycle on Titan is both impacted by tropospheric dynamics and likely able to impact this circulation via feedbacks. Here we use the 3D TitanWRF General Circulation Model (GCM) to simulate Titan's methane cycle. In this initial work we use a simple large-scale condensation scheme with latent heat feedbacks and a finite surface reservoir of methane, and focus on large-scale dynamical interactions between the atmospheric circulation and methane, and how these impact seasonal changes and the long term (steady state) behavior of the methane cycle. We note five major conclusions: (1) Condensation and precipitation in the model is sporadic in nature, with interannual variability in its timing and location, but tends to occur in association with both (a) frequent strong polar upwelling during spring and summer in each hemisphere, and (b) the Inter-Tropical Convergence Zone (ITCZ), a region of increased convergence and upwelling due to the seasonally shifting Hadley cells. (2) An active tropospheric methane cycle affects the stratospheric circulation, slightly weakening the stratospheric superrotation produced. (3) Latent heating feedback strongly influences surface and near-surface temperatures, narrowing the latitudinal range of the ITCZ, and changing the distribution – and generally weakening the strength – of upwelling events. (4) TitanWRF favors low latitude 'cloudiness' around northern spring equinox as the ITCZ moves from south to north across the equator, versus the opposite time of year. (5) TitanWRF produces drying of low and mid latitudes with net transport of surface methane to high latitudes, and shows persistent hemispheric asymmetry in the methane cycle such that the favored pole for surface methane is the one with winter occurring closest to perihelion.

© 2015 Elsevier Inc. All rights reserved.

1. Introduction

For several decades, observations of methane have suggested the presence of a methane hydrological cycle on Titan (Kuiper, 1944; Hanel et al., 1981; Tyler et al., 1981). Methane clouds were first inferred from telescopic observations of brightness changes in methane windows that saw down to the troposphere, with estimates of the altitudes involved matching those expected for methane convective clouds (Griffith et al., 1998, 2000). Subsequent imaging showed that the brighter areas were confined to high southern (summer) latitudes (Brown et al., 2002; Roe et al., 2002; Bouchez and Brown, 2005; Schaller et al., 2006a). Continued monitoring produced further data on the seasonal variation in both cloud activity and location, with clouds observed at increasingly low latitudes toward equinox (Roe et al., 2005; Schaller et al., 2009) and activity almost ceasing for several Earth months in mid southern summer (Schaller et al., 2006b). Cassini instruments provided further evidence of activity from 2004 onwards, with clouds observed by the Visual Mapping Infrared Spectrometer (VIMS) and Imaging Science Subsystem (ISS) instruments (Griffith et al., 2005, 2009; Turtle et al., 2009, 2011a, 2011b). Although both Earth-based and Cassini observations have coverage

* Corresponding author.
E-mail addresses: claire@aeolisresearch.com (C.E. Newman), mir@aeolisresearch.com (M.I. Richardson), lian@aeolisresearch.com (Y. Lian), lee@aeolisresearch.com (C. Lee).

http://dx.doi.org/10.1016/j.icarus.2015.11.028
0019-1035/© 2015 Elsevier Inc. All rights reserved.

issues, and the latter began in mid 2004, well after southern summer solstice (planetocentric solar longitude, $L_s = 270°$, which occurred in October 2002), to date the overall pattern appears to be: (i) frequent summer hemisphere high-latitude cloud activity within ~60° of L_s of solstice; (ii) increased, though patchier, cloud activity at summer mid-latitudes following solstice while the high-latitude cloud activity continues; (iii) a decline in high latitude cloud activity, with infrequent clouds observed in mid and low latitudes, as Titan passes through equinox toward the opposite solstice (northern spring equinox, $L_s = 0°$, occurred in August 2009, while northern summer solstice, $L_s = 90°$, will occur in May 2017). Observations are complicated by uncertainty as to the composition of the thick polar hood clouds that develop over the winter pole. These have been largely attributed to condensation of high-altitude ethane advected into the winter polar vortex at upper levels by the large-scale overturning circulation (e.g. Griffith et al., 2006), though it is possible that methane condensation (perhaps around ethane ice cores) in the lower stratosphere also plays a role in their thickness and depth (Anderson et al., 2012).

Lakes are observed at high latitudes in both hemispheres by Cassini Radar and other imaging (Stofan et al., 2007; Hayes et al., 2008; Sotin et al., 2012), with far larger lakes and greater areal coverage in the northern hemisphere, where some shorelines extend down as far as 50°N. The detection of ethane by VIMS in Ontario Lacus (Brown et al., 2008) and photochemical calculations of likely lake constitution (e.g., Cordier et al., 2009, 2013) suggest that this southern lake is likely only ~10% methane (by mole fraction) and ~75% ethane, whereas recent Radar observations of Ligeia Mare, one of the large northern lakes, suggests that it may be mostly composed of methane (Zebker et al., 2014). The hemispheric lake asymmetry has been linked to the occurrence of perihelion (the time of greatest solar insolation) near southern summer solstice, resulting in greater net methane accumulation (more precipitation than evaporation) over the longer, cooler summer experienced by northern high latitudes (Aharonson et al., 2009; Schneider et al., 2012). This may be analogous to the trapping of minor species volatiles at the aphelion pole on Mars (Richardson and Wilson, 2002; Montmessin et al., 2007). Recent observations also suggest small changes in lake levels since Cassini arrived at Titan, either due to evaporation or infiltration into the surface (e.g. Hayes et al., 2011; Turtle et al., 2011b). Past rainfall is suggested by the pattern of flow features on the surface at the Huygens landing site (e.g. Tomasko et al., 2005), while recent surface change at both low and high latitudes detected by the Cassini ISS instrument has also been attributed to rainfall (Turtle et al., 2009, 2011a, 2011c).

To fully understand the nature of Titan's methane cycle and its interaction with Titan's atmospheric dynamics it is necessary to employ a General Circulation Model (GCM). Mitchell et al. (2006, 2009, 2011), Mitchell (2008) and Schneider et al. (2012) implemented a basic methane cycle in troposphere-only GCMs, which were radiatively forced using simple gray radiative transfer schemes. In the case of Mitchell et al. (2009) and Mitchell (2008) the model used was also 2D or axisymmetric (i.e., had no longitudinal dimension and thus did not permit eddies). Tokano et al. (2001) examined the methane cycle in a 3D GCM extending from the surface through the stratosphere, though their model did not include realistic stratospheric superrotation. Rannou et al. (2004) and Rodriguez et al. (2009) modeled the methane cycle in the IPSL 2D Titan GCM, which extends over a similar vertical range and includes a zonal mean methane microphysics scheme. Although this 2D model cannot explicitly represent eddies, the amount of eddy activity is predicted based on the diagnosed barotropic instability, with the associated mixing parameterized using a relationship obtained from a 3D GCM run in a shallow water configuration (Luz and Hourdin, 2003; Luz et al., 2003). Most recently, Lora et al. (2015) produced Titan methane cycle simulations using a 3D GCM extending up to the lower mesosphere.

Here we use the 3D TitanWRF GCM to simulate Titan's methane cycle. This model produces strong stratospheric superrotation, thus provides a more realistic upper boundary condition for the tropospheric circulation, as does Lora et al. (2015). We focus on large-scale dynamical interactions between the atmospheric circulation and methane, and how these impact seasonal variation and the long term (steady state) behavior of the methane cycle. We do not include full microphysics, photochemistry or advected haze, thus do not consider the impact of interactions between haze particles and the ethane and methane cycles. The reasons for this are twofold: (i) including more detailed feedbacks was premature for this study and would have complicated the analysis of our results, and (ii) the additional time required for detailed microphysical calculations was incompatible with the need to run very long simulations (lasting many tens of Titan years) in order to approach steady state behavior.

In the remainder of this paper, unless specified otherwise, 'year' refers to one Titan year, 'day' to a Titan solar day, with ~673 days per year and one day lasting 15.95 Earth days, and 'hour' to a Titan hour, which is equal to 1/24th of a day and lasts 15.95 Earth hours.

2. The TitanWRF General Circulation Model and simple methane cycle scheme

2.1. Model description

The TitanWRF GCM is the Titan version of the planetWRF GCM (version 3.0.1.2) developed from the terrestrial Weather, Research and Forecasting (WRF) model (Skamarock et al., 2005). A general description of planetWRF is given in Richardson et al. (2007), with details of the version of TitanWRF used in this work provided in Newman et al. (2011), so here we present only a brief description of key model aspects before focusing on the physical parameterizations added to TitanWRF to perform methane cycle simulations.

2.1.1. The dynamical core

TitanWRF solves the 3D primitive equations using a finite-difference method on a standard Arakawa C-grid. It utilizes a longitude–latitude horizontal grid evenly spaced at 5.625° in longitude and 5° in latitude, and a terrain-following, modified-sigma vertical coordinate σ' in the vertical, with 54 layers from the surface to ~420 km, where $\sigma' = (P - P_{top})/(P_{surf} - P_{top})$ and P = pressure. A latitude-dependent polar filter is applied polewards of 45°, gradually damping more wavenumbers as the zonal spacing decreases with latitude, to prevent numerical instabilities from developing near the poles where the zonal grid points converge. TitanWRF employs a physical boundary condition at the surface (i.e., exchanges angular momentum via drag between the atmosphere and surface). It also includes Rayleigh drag in the top four model layers (the 'sponge layer') to damp growing wave amplitudes and reduce wave reflections, both of which are sources of numerical instabilities. In the sponge layer, horizontal winds are relaxed to the zonal mean over timescales that gradually decrease from 6 days to 1 day toward the model top.

TitanWRF is currently run with no explicitly-imposed horizontal diffusion, which is typically added to maintain stability and parameterize the effect of mixing by sub-grid scale eddies. In past work we found the production of stratospheric superrotation to be greatly impeded by overly-strong horizontal mixing of heat and momentum, and determined that the strongest and most realistic superrotation was produced with no explicit horizontal mixing at all (Newman et al., 2011). Such mixing interfered with the low/mid latitude barotropic waves that transported negative angular

momentum out of the equatorial region, which were crucial to the production and maintenance of equatorial superrotation in the stratosphere. TitanWRF still includes implicit 6th-order horizontal diffusion, associated with its 5th-order finite difference solver, which appears sufficient to suppress spurious grid-scale oscillations in temperature and wind. Thus the dynamical core still includes some horizontal mixing without adversely impacting the generation of eddies and their interaction with the mean flow. Newman et al. (2011) showed comparisons with observations, demonstrating that TitanWRF produced peak zonal winter jet velocities and seasonal changes comparable to those inferred from Cassini CIRS stratospheric temperature retrievals (Achterberg et al., 2008, 2011). For the Huygens entry season and location, TitanWRF did not capture the large observed zonal wind minimum centered at ~90 km altitude, though produced a closer match to observations above 120 km and showed reasonable agreement with winds in the lower troposphere.

2.1.2. Existing parameterizations of physical processes

Methane vapor transport in TitanWRF is carried out by a 5th order in the horizontal, 3rd order in the vertical and 4th order in time Runge–Kutta advection scheme, with additional positive-definite and mass conservation constraints employed. This scheme also provides implicit horizontal mixing, as described in the previous paragraph. TitanWRF's vertical diffusion scheme, which parameterizes the vertical diffusion of heat, momentum and tracers (here methane vapor) both within and above the planetary boundary layer, is adapted from the existing 'MRF' scheme already inside WRF (Hong and Pan, 1996). This scheme accounts for both local and non-local vertical diffusion, with the former parameterized via a simple diffusion equation and constant diffusion coefficient that depends on the atmospheric stability profile, and the latter parameterized (within the boundary layer only) via the addition of a factor again determined by atmospheric stability. Boundary layer height is determined by a critical Richardson number below which convective instability supersedes shear instability. The MRF scheme was chosen due to its relative simplicity and lack of empirically-derived parameters (which are quite common in Earth-based boundary layer schemes).

TitanWRF uses a two-stream radiative transfer model to determine heating rates at visible and infrared wavelengths. Gas and haze optical properties are found using a modified version of the scheme described by McKay et al. (1989, personal communication, 2004–2006). The scheme used in this work does not include haze microphysics or advection. Instead, for each radiative timestep (every half hour), a haze particle size and number concentration is estimated at each grid point using a simple 1D scheme that balances coagulation and sedimentation of small upper level source particles (McKay et al., 1989).

TitanWRF allows the surface temperature to evolve in response to the exchange of radiative and sensible heat with the atmosphere and sub-surface. It includes a surface/sub-surface scheme that deals with the exchange of heat, tracers (here methane vapor), and momentum between the surface and atmosphere, and includes the diffusion of heat through 12 sub-surface layers assuming that the lowest layer (centered at a depth of 5.53 m) has a fixed temperature of 94 K. The scheme does not currently include the sub-surface vertical diffusion of methane. In the present work we treat Titan's surface as flat. Titan's albedo, surface density (ρ_{surf}), specific heat capacity (c_p^{surf}), and thermal inertia (TI) are also assumed to be globally uniform with values of $A = 0.32$, $\rho_{surf} = 800$ kg m^{-3}, $c_p^{surf} = 1400$ J kg^{-1} K^{-1} and TI = 335 J m^2 s$^{-1/2}$ K^{-1}, respectively. This gives a thermal conductivity $\kappa = 0.1$ W m^{-1} K^{-1}, via TI = $(\rho_{surf} c_p^{surf} \kappa)^{1/2}$. Uniform surface properties were partly employed due to lack of global coverage to infer maps (though some maps now exist, e.g. of topography (Lorenz et al., 2013)), but also in the interests of keeping our initial methane cycle experiments relatively straightforward in terms of understanding the mechanisms at work. TI and its component values were set to those chosen by Tokano (2005) for his porous icy regolith surface type (based mainly on Kossacki and Lorenz (1996)), and this TI value is consistent with (albeit at the lower end of) the range inferred from CIRS low-latitude surface temperature observations (Cottini et al., 2012), for which the diurnal change of ~1.5 K coupled with their model predictions suggested a TI between 300 and 600 J m^2 s$^{-1/2}$ K^{-1}. As discussed in Section 5, however, a higher TI appears necessary to match temperature observations when latent heating (evaporative cooling) is active at the surface. The albedo chosen produces the best match to Voyager temperature observations using the 1D McKay et al. (1989) radiative transfer code (which forms the basis of the code used in TitanWRF), and is slightly smaller (implying more surface absorption of solar radiation) than the value of 0.38 used by Tokano (2005) for his porous icy regolith surface type.

2.2. Additional methane cycle parameterizations required for this work

In addition to advection and mixing (described above), the methane cycle also requires us to represent (a) atmospheric condensation/evaporation and associated latent heating/cooling of the atmosphere, (b) surface precipitation, and (c) surface evaporation and associated latent cooling of the surface. The parameterizations of these processes are described below.

2.2.1. Large-scale condensation and precipitation

In the TitanWRF scheme, condensation occurs when the vapor pressure of methane, P_{CH4}, exceeds the saturation vapor pressure, P_{sat}; i.e., when the relative humidity ($100P_{CH4}/P_{sat}$) = 100%. In reality, the presence or absence of suitable cloud condensation nuclei (CCN) may affect the threshold of critical relative humidity, e.g. condensation may occur even when the atmosphere is subsaturated if significant CCN are present and there is embedded small-scale vertical motion, or not occur when the atmosphere is super-saturated if nucleation is CCN-limited (though the latter seems unlikely given the abundance of haze particles falling from above). Here we allow condensation to occur at 100% saturation for simplicity. The saturation vapor pressure and the type of condensate that forms are determined by the atmospheric temperature, T, with four different temperature regimes possible:

$$(1)\ T_{CH4}^{crit} < T: \text{ no condensation occurs} \tag{1a}$$

where T_{CH4}^{crit} is the critical temperature of methane = 190.53 K.

$$(2)\ T_{N2}^{crit} < T < T_{CH4}^{crit}: \text{ condensate is liquid methane} \tag{1b}$$

$$P_{sat} = P_{sat}^{CH4liq} = 10^5 \times 10^{\wedge}(3.901408 - 437.54809/T + 1598.8512/T^2 - 154567.02/T^3)$$

from Moses et al. (1992), where T_{N2}^{crit} is the critical temperature of nitrogen = 126.2 K.

$$(3)\ T_{CH4}^{trip} < T < T_{N2}^{crit}: \text{ condensate is binary solution of methane and nitrogen} \tag{1c}$$

$$P_{sat} = \gamma_{CH4} X_{CH4} P_{sat}^{CHliq} / F_{CH4}$$

where T_{CH4}^{trip} is the triple point of methane = 90.68 K. We assume the nitrogen mole fraction of the condensate, X_{N2}, is constant and =0.2, giving a constant methane mole fraction of the condensate, $X_{CH4} = 1 - X_{N2} = 0.8$. We also assume the fugacity coefficient, F_{CH4}, is constant and =0.95. We set these values based on a typical tropospheric profile (Thompson et al., 1992) to avoid the complexity

involved in finding iterative solutions, which vary anyway depending on the model used (Kouvaris and Flasar, 1991; Thompson et al., 1992). We further assume that only a binary solution forms, though in reality a non-binary solution may exist depending on the methane partial pressure. We calculate the activity coefficient, γ_{CH4}, using:

$$\gamma_{CH4} = \exp\hat{}\{X_{N2}^2 \times [(a - 3b + 5c) + 4(b - 4c)X_{N2} + 12cX_{N2}^2]\}$$

where $a = 0.8096 - 52.07/T + 5443/T^2$, $b = -0.0829 + 9.34/T$, and $c = 0.0720 - 6.27/T$.

(4) $T < T_{CH4}^{trip}$: condensate is methane ice (1d)

$$P_{sat} = P_{sat}^{CH4ice} = 10^5 \times 10\hat{}(4.425070 - 453.92414/T - 4055.6016/T^2 + 115352.19/T^3 - 1165560.7/T^4)$$

from Moses et al. (1992). Note that we neglect here the suppression of the freezing point for a binary methane–nitrogen mixture, which may enable binary liquid condensation at temperatures considerably (by ~10–15 K) lower than the methane triple point (at 90.68 K).

Once condensation occurs it is not transported by the advection scheme, nor do we form cloud particles (e.g., we do not represent the condensate as a particle size distribution with different sedimentation speeds). Instead we assume that all of the condensate reaches the surface unless there are sub-saturated layers below the condensation level, in which case enough is re-evaporated in order to saturate them (starting with the highest and working down the atmospheric column). Any condensate remaining by the surface is tracked as precipitation and added to the surface methane budget. The absence of detailed cloud microphysics means we cannot properly represent most cloud processes or include the coupling between the haze, ethane and methane distributions (e.g., ethane ice nucleation around haze particles; methane condensation around ethane ice or haze). This is a major shortcoming of the current study, but as noted in Section 1 it would be too computationally expensive for TitanWRF simulations lasting several Titan decades (~an Earth millenia). In addition, the large number of assumptions, parameters and processes involved in such schemes would complicate the analysis of results, making them of limited use for these initial GCM studies, which are focused on understanding dynamical interactions and feedbacks.

2.2.2. Surface evaporation

We calculate surface methane evaporation, Ev_{CH4} (in kg m^{-2}), using the bulk-aerodynamic formula of Deardorff (1972), as in Tokano et al. (2001). Evaporation is given by:

$$Ev_{CH4} = \min(Surf_{CH4}, \max[C_{drag}(Q_{sat} - Q_{CH4})M_{fact}\delta t, 0]) \quad (2)$$

where $Surf_{CH4}$ is the surface methane (in kg m^{-2}), C_{drag} is the surface exchange coefficient calculated from the GCM's surface layer scheme (see Section 2.1.2), Q_{sat} and Q_{CH4} are respectively the saturation mass mixing ratio (mmr) and mmr of methane vapor in the lowest atmospheric layer, M_{fact} is the surface moisture availability factor, and δt is the model timestep (~400 s). Q_{sat} is found from P_{sat} by:

$$Q_{sat} = R_{hum}P_{sat}M_{rat}/P$$

where R_{hum} is the relative humidity chosen for condensation to occur (here 100%), M_{rat} is the ratio of mean molecular masses of methane and Titan's background atmosphere, ~16/27, and P is the pressure at the middle of the lowest atmospheric layer. $Surf_{CH4}$ is tracked in according to past precipitation (Pr_{CH4}) and evaporation at each grid point, i.e.:

$$Surf_{CH4} = Surf_{CH4}^{init} + \text{sum of } (Pr_{CH4} - Ev_{CH4}) \text{ over all previous timesteps.}$$

Note that M_{fact} does not refer to the amount of methane at the surface but rather the ease with which surface methane may be evaporated, which will depend on the type of surface on/in which the methane resides (e.g., adsorbed into a porous regolith versus a rocky regolith, or held in a lake). $M_{fact} = 0$ corresponds to a surface in which methane is permanently trapped, whereas $M_{fact} = 1$ corresponds to methane on top of the surface with no barrier to evaporation. Here we do not track surface type, so we assume that $M_{fact} = 0.5$ everywhere, equivalent to assuming that surface methane is partially adsorbed into the top regolith layer, as opposed to e.g. forming a liquid lake or diffusing deeper into the sub-surface. Given the many other approximations and uncertainties involved in these simulations, this is a reasonable starting point, but we will explore the sensitivity to M_{fact} in future work as a prelude to including a Land Surface Model (LSM) into TitanWRF (for details see Section 6.4).

2.2.3. Latent heating/cooling in the atmosphere and at the surface

In this work we ignore the radiative impact of varying the distribution of gaseous or condensed methane. Instead, TitanWRF's radiative transfer scheme sees a fixed, prescribed methane distribution based on Voyager observations (Lellouch et al., 1989). However, we do consider the latent heating/cooling associated with condensation/evaporation of methane. We calculate the heat gained/lost when atmospheric methane condenses/evaporates using either the latent heat of methane evaporation, L_{CH4}^{liq}, for liquid and binary clouds, or the latent heat of methane sublimation, L_{CH4}^{sub}, for ice clouds. As in Barth and Toon (2006):

$$L_{CH4}^{liq} = (437.54809 - 3197.7024/T + 463701.06/T^2)R_d \ln(10)/M_{CH4}$$

$$L_{CH4}^{sub} = (453.92414 + 8111.2032/T - 346056.57/T^2 + 4662242.8/T^3]R_d \ln(10)/M_{CH4}$$

where R_d is the gas constant = 8.314, and M_{CH4} is the molar mass of methane in kg mol^{-1} (16×10^{-3}). The predicted temperature change per timestep, δT, is then given by:

$$\delta T = L_{CH4}\delta Q_{CH4}/c_p$$

where δQ_{CH4} is the change in methane mmr over the timestep, and c_p is the specific heat capacity at constant pressure in Titan's atmosphere = 1044 J K^{-1} kg^{-1}. We similarly calculate the heat removed when surface methane is evaporated, δT_{surf}, using:

$$\delta T_{surf} = -L_{CH4}Ev_{CH4}/(c_p^{surf}\rho_{surf}\delta z_{surf})$$

where $\delta z_{surf} = 0.012$ m is the depth of the GCM's uppermost subsurface layer.

The latent heating/cooling rates shown above are calculated based on the condensation or evaporation predicted given the current state of the atmosphere, and are then applied across a model timestep (~400 s). These rates will be invalid if condensation/evaporation and resultant heating/cooling would have changed the atmospheric state significantly within this time period (i.e., if the true condensation/evaporation timescales are much shorter than the model timestep). This is not usually a major concern, and in the atmosphere the vertical diffusion scheme described in Section 2.1.2 is able to mimic convection by mixing heat, momentum and tracers more vigorously if the profile becomes unstable, tending to prevent large vertical gradients in potential temperature developing when condensation occurs. If particularly strong condensation/evaporation occurs, however, the calculated heating/cooling in a single timestep may be far larger than would occur in reality, even producing instabilities in the model. This problem may be dealt with explicitly by the addition of 'sub-timesteps' which are much shorter and allow updates to occur more

frequently, or implicitly by slowing the condensation/evaporation process such that its timescales are now comparable to a model timestep and the rest of the model dynamics. A related problem is that in a real atmosphere cloud processes take place at much finer spatial scales than in a ~5° resolution GCM. To treat them correctly we would need to run the global model at ~10–100 m resolution with very short timesteps, which is completely impractical for all current climate modeling systems.

Possible solutions to these issues would be to apply a moist convection parameterization in the atmosphere and a sub-timestepping scheme at the surface. The goal of a moist convection parameterization is to parameterize the large-scale fluxes of vapor, condensate, and heat that would be produced by real clouds, based on the large-scale atmospheric state. A simple version of such a parameterization is a moist convective adjustment (MCA) scheme, in which relative humidity is relaxed toward a prescribed relative humidity profile over a pre-determined timescale, thus controlling the rate of latent heat release. MCA schemes have been used in some Titan methane cycle investigations (e.g. Mitchell et al., 2006; Schneider et al., 2012; Lora et al., 2014). However, a more physically-based method of parameterizing moist convection is preferable, and we discuss this further in Section 6.4.

In the present work we use only a large-scale condensation scheme and vertical diffusion scheme. To prevent the rare model instabilities that may develop we also limit the maximum condensation or evaporation rate per timestep in the atmosphere and at the surface, such that they produce maximum atmospheric and surface temperature changes of δT_{atm} and δT_{surf} respectively, implicitly placing a cap on how fast these processes can occur. The default values of δT_{atm} and δT_{surf} are 0.01 K s^{-1}, i.e. a maximum temperature change of nearly 4 K per model timestep. This approach is more an *ad hoc* numerical solution to prevent instabilities than an attempt to parameterize a physical process, but it does not significantly impact the overall results as the latent heating rate only rarely exceeds these imposed upper limits.

2.3. Simulations included in this paper

We begin by briefly examining the 'passive' methane cycle without latent heating feedbacks, in which the circulation is unaffected by the methane cycle (Section 3.1.1). We examine the methane cycle produced assuming infinite surface methane availability (simulation INF, Section 3.1.2), then with more realistic finite surface methane availability (FIN, Section 3.1.3). We next include latent heating feedbacks and examine the 'active' methane cycle (FIN_LH, Section 3.2), comparing the simulated circulation and methane cycle with observations. We then focus on the causes of the observed and simulated hemispheric asymmetry in surface methane, and show that it reverses when we reverse the timing of perihelion (FIN_LH_RP, Section 4). Finally, we look at the impact of increasing the surface thermal inertia (FIN_LH_TI, Section 5). These simulations are summarized in Table 1. Unless noted otherwise, all simulations are initialized from the end of the fully spun-up (75-year) TitanWRF simulation shown in Newman et al. (2011), which has realistic stratospheric superrotation, and then run until an atmospheric or full steady state methane cycle is achieved – i.e., until respectively the atmospheric or atmosphere + surface seasonal methane cycle roughly repeats each year, and no further long term changes occur.

Table 1
Summary of TitanWRF simulations used in this paper. See text for details.

Name	Active	Finite surface methane	Perihelion (in ° L_s)	Thermal inertia (in J m^2 $s^{-1/2}$ K^{-1})
INF	No	No	279	335
FIN	No	Yes	279	335
FIN_LH	Yes	Yes	279	335
FIN_LH_RP	Yes	Yes	99	335
FIN_LH_TI	Yes	Yes	279	2711

3. Results

3.1. Passive methane cycle results

The passive simulations (INF and FIN) do not include latent heating/cooling due to methane condensation/evaporation. Their dynamics are therefore identical to each other, and to those in Newman et al. (2011), although here we focus on the troposphere whereas that paper focused on the stratosphere. These results provide a baseline for our later results, and allow us to explore the methane cycle's response to the seasonally-evolving solar insolation in the absence of latent heating feedbacks which – although more realistic – greatly complicate the analysis. As noted in Section 2.2.3, we do not include radiative feedbacks associated with changes to the atmospheric methane distribution in any simulation.

3.1.1. The tropospheric circulation with a passive methane cycle (INF or FIN)

Fig. 1a shows the seasonal evolution of zonal mean shortwave heat flux into the surface (in W m^{-2}) averaged over four years of one of the passive methane simulations (INF or FIN, henceforth referred to as 'INF/FIN'). The peak heating at mid-latitudes rather than at the poles in local summer is due to the greater along-path atmospheric optical depth (between the Sun and Titan), resulting in more absorption of the incoming solar flux, as latitude increases (Lora et al., 2011). Note that this effect is omitted from several GCM simulations used to study Titan's methane cycle (e.g. Mitchell et al., 2006; Tokano, 2005; Schneider et al., 2012). Saturn's orbital eccentricity is evident in the bias between northern and southern summer, with the latter receiving more heating due to the presence of perihelion (time of closest approach to the Sun) at $L_s \sim 279°$, just after southern summer solstice. The horizontal axis shows planetocentric solar longitude, L_s, so is not linear in time, and in fact the warmer southern summer lasts only 155 days while the cooler northern summer lasts 181 days.

Fig. 1b shows the seasonal variation in zonal mean surface temperatures averaged over four years of INF/FIN. The surface temperature peaks at ~93 K at the north pole in northern summer and ~0.5 K higher at the south pole in southern summer, with minimum temperatures of ~88.5 K at both poles in local winter. Note that this temperature is below the freezing point of methane (Section 2.2.1), and this was one of the factors that led to us examining results with an increased thermal inertia, as described in Section 5. Fig. 2 shows a comparison between CIRS surface temperatures measured at two times of year (symbols; taken from Jennings et al. (2009, 2011)) and those simulated by INF/FIN (solid red and blue lines). Overall the latitudinal range in surface temperatures is comparable and the simulation reproduces the northern hemisphere warming and southern hemisphere cooling as Titan moves from northern winter into spring, though the mean temperature is slightly cooler than observed (by <1 K). Both simulated and observed temperatures peak near the equator in spring, but in late winter they peak in the summer hemisphere only in the simulation.

Fig. 3 shows the mass streamfunctions, zonal mean temperatures, and zonal mean zonal winds for northern hemisphere spring, summer, autumn and winter, averaged over four years of simulation INF/FIN. Temperature shows the subtlest changes with season. Peak near-surface temperatures shift from the

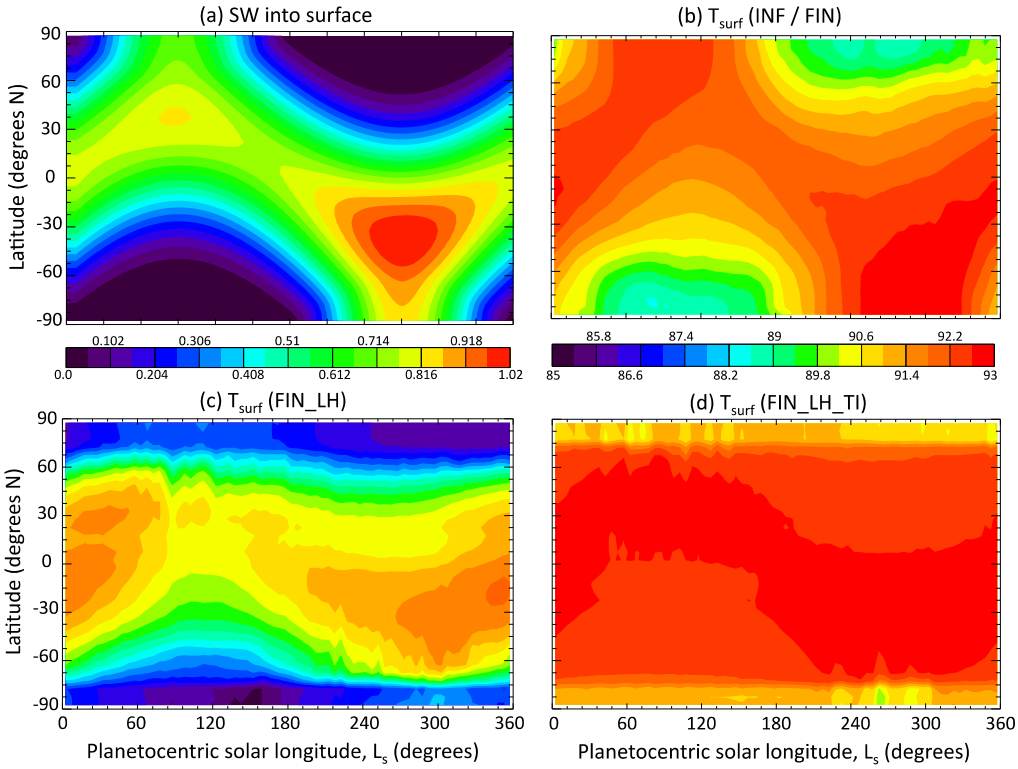

Fig. 1. (a) Zonal mean shortwave heat flux into the surface (in W m^{-2}) as a function of latitude and planetocentric solar longitude (L_s) for one year of a TitanWRF simulation. (b–d) Zonal mean surface temperature (in K) as a function of latitude and L_s, averaged over the last four years of simulations (b) INF/FIN, (c) FIN_LH, and (d) FIN_LH_TI. The left hand contour bar refers to plot (a), the right hand contour bar to plots (b–d).

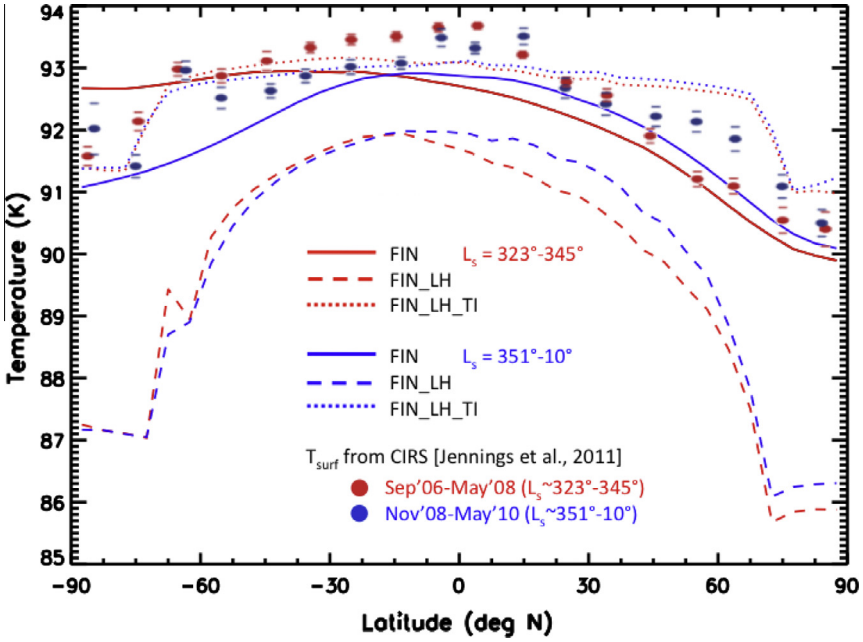

Fig. 2. Surface temperatures as a function of latitude observed at two times of year by CIRS (symbols) (Jennings et al., 2009, 2011) and simulated at the same times of year by simulations FIN (sold lines), FIN_LH (dashed lines) and FIN_LH_TI (dotted lines). Red is September 2006–May 2008 ($L_s \sim 323$–$345°$); blue is November 2008–May 2010 ($L_s \sim 351$–$10°$). (For interpretation of the references to color in this figure legend, the reader is referred to the web version of this article.)

equator at equinox (e.g. Fig. 3b) to high summer latitudes at solstice (e.g. Fig. 3e). Enhanced temperature gradients in winter and spring high latitudes are associated with stronger positive zonal winds forming a circumpolar westerly jet (e.g., in the south in Fig. 3e and f, for temperature and zonal wind respectively). The streamfunction plots show classic Hadley-type overturning circulations, with a double cell rising at low latitudes and descending in mid to high latitudes around equinox (Fig. 3d and j), and with a very broad single cell extending from high winter latitudes to mid summer latitudes around solstice (Fig. 3a and g). Other key features are the strong polar cells associated with the low pressure system that develops inside the winter circumpolar jet.

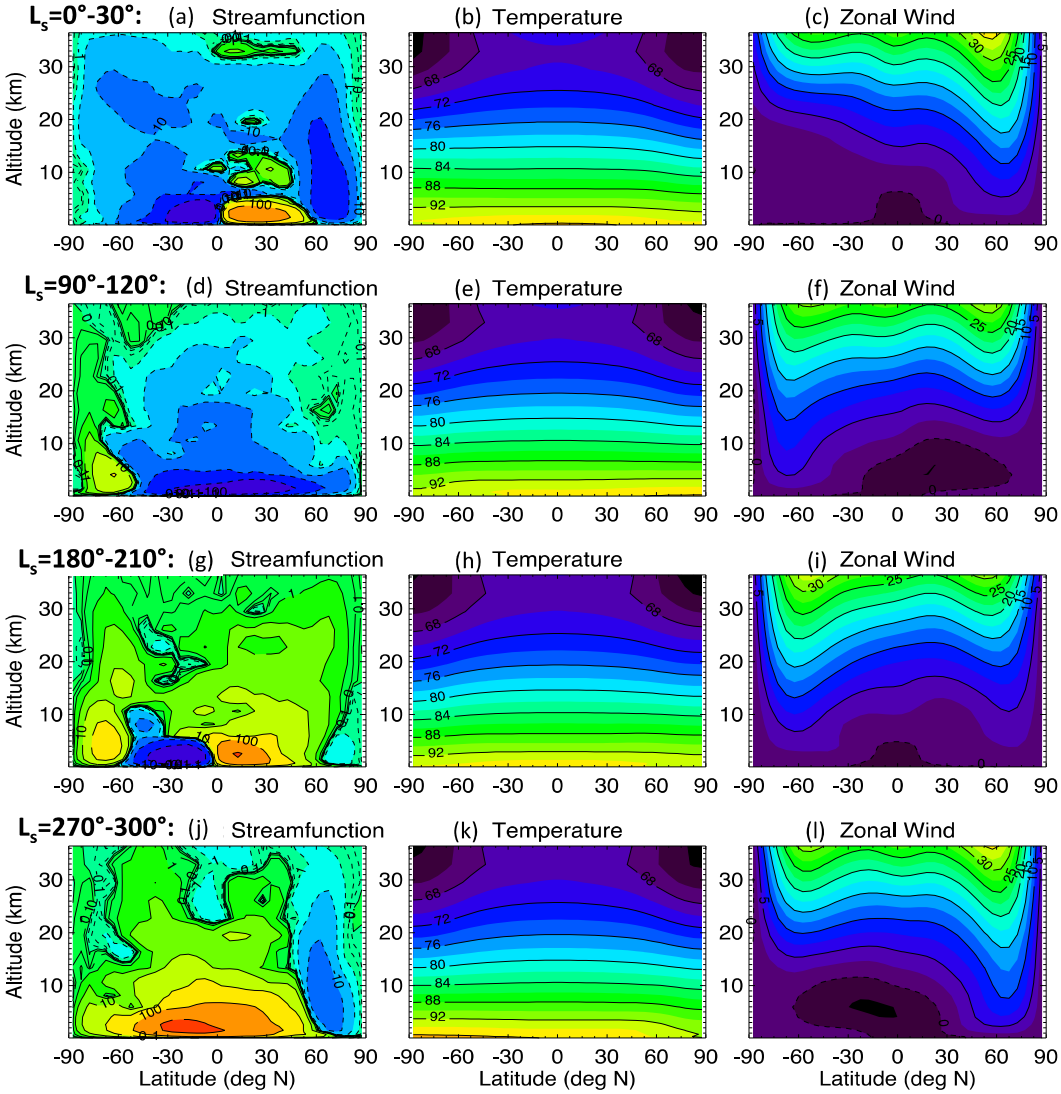

Fig. 3. The tropospheric circulation in a passive methane simulation (INF/FIN). Left column: mass streamfunction (in kg s^{-1}; solid lines and yellow/red shading are clockwise meridional circulations, dashed lines and blue/purple shading are counterclockwise). Middle column: zonal mean temperature (in K). Right column: zonal mean zonal wind (in m s^{-1}; positive values are winds to the east). Results are averaged over four years in the following periods: Top row: northern spring (L_s = 0–30°); second row: northern summer (L_s = 90–120°); third row: northern autumn (L_s = 180–210°); bottom row: northern winter (L_s = 270–300°). (For interpretation of the references to color in this figure legend, the reader is referred to the web version of this article.)

These cells consist of rising motion over the poles and descending motion in mid-latitudes in local winter and spring (see the clockwise circulation at high southern latitudes for L_s = 90–120° and 180–210°, Fig. 3d and g, and the anticlockwise circulation at high northern latitudes for L_s = 270–300° and 0–30°, Fig. 3j and a), with the stronger northern hemisphere polar cell even visible in autumn (L_s = 180–210°, Fig. 3g). These polar cells produce strong upwelling over the winter and spring pole, in addition to the upwelling due to the upward Hadley cell branch that extends to high latitudes in summer. In combination, these features drive strong methane condensation over much of the year at both poles, which dominates the methane cycle in these simulations (see Section 3.1.2).

Fig. 4a shows the seasonal evolution of the maximum tropospheric zonal mean vertical velocity, w_{max}, averaged over 4 years of simulation INF/FIN. The dominant feature is the strong upwelling at high latitudes from local late winter through early summer, associated with the polar cells described above. Although there is some interannual variability (not shown), upwelling peaks consistently in late spring, at $L_s \sim 70°$ in the north and $L_s \sim 250°$ in the south, although strong northern upwelling also occurs in late winter. As first described by Mitchell et al. (2006), peak upwelling in mid to low latitudes is roughly associated with the location of the Hadley circulation's upwelling branches – the Inter-Tropical Convergence Zone (ITCZ) – which moves between summer high latitudes each year, crossing the equator just after the equinoxes. Interestingly, the maximum zonal mean upwelling in the ITCZ is far weaker than that produced by the polar cells.

Fig. 4b shows the zonal mean divergence of the near-surface meridional flow, $dv/d\phi$, where v is meridional velocity and ϕ is latitude, averaged over four years of simulation INF/FIN. Strong meridional convergence associated with the ITCZ appears as large negative values. Although the streamfunction plots suggest the upward branch of the solsticial Hadley circulation begins at the summer pole (i.e., at the north pole at L_s = 90°, Fig. 3d, and at the south pole at L_s = 270°, Fig. 3j), the width of the ITCZ revealed here may be slightly smaller and appears 'diluted' polewards of ~60° latitude in local summer, probably due to interference from localized patches of strong convergence and divergence associated with the strong polar cells.

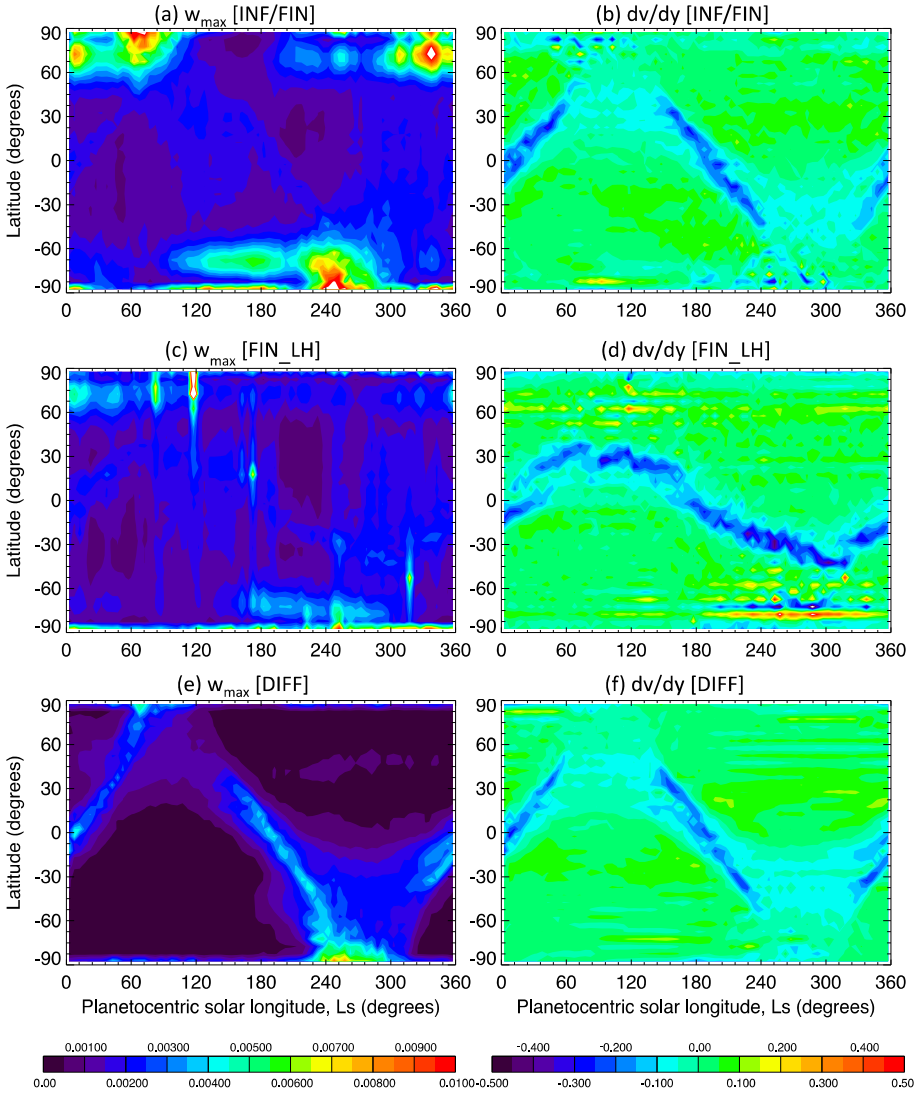

Fig. 4. Left column (a, c, and e): zonal mean maximum vertical velocity in the troposphere, w_{max} (in m s^{-1}). Right column (b, d, and f): zonal mean near-surface meridional divergence, $dv/d\phi$ (in units of m s^{-1} rad^{-1}). Results are shown as a function of latitude and L_s, averaged over the last four years of simulations (a and b) INF/FIN (passive methane), (c and d) FIN_LH, and (e and f) a passive methane simulation with explicit horizontal diffusion. Contour levels are chosen so that the largest magnitudes 'saturate' to emphasize the smaller values outside of high latitudes. Note that although plotting the maximum vertical velocity highlights regions of upwelling, equal downwelling occurs in a global mean sense.

3.1.2. The passive methane cycle assuming infinite surface methane (simulation INF)

In practice, simulation INF was initialized with a finite, globally-uniform surface methane abundance of 1×10^5 kg m^{-2} (giving a globally-uniform depth of ~222 m assuming a liquid methane density of 450 kg m^{-3}), but this was large enough that no surface region was exhausted during the 7 year simulation, making the surface methane supply effectively infinite. The methane cycle reached an *atmospheric* steady state after 3 years, and simulation INF was then run for another 4 years to produce the results shown. While INF is not in a *full* (atmosphere + surface) steady state by its end (since surface methane continues to show long term changes) we use it to briefly examine the methane cycle that would be produced by the passive circulation if surface methane availability were not a factor.

Fig. 5 shows the seasonal evolution of (a) tropospheric column methane and (b) near-surface methane, averaged over 4 years of INF. Peak values follow the seasonal evolution of peak meridional convergence in the ITCZ shown in Fig. 4b, indicating that tropospheric methane is concentrated by the converging lower branches of the Hadley cells, as discussed in Mitchell et al. (2006). In local autumn and winter ($L_s \sim 180$–$360°$ in the north, ~0–180° in the south), the strong polar vortex cuts off transport of methane to high latitudes and keeps abundances there relatively low, particularly in the north. In spring the polar vortex breaks down, allowing more methane to reach high latitudes. However, strong polar upwelling (large w_{max} in Fig. 4a) peaking in late spring/early summer ($L_s \sim 50$–$100°$ in the north, ~230–280° in the south) advects methane up and out of the polar region, drying the atmospheric column and the lowest layer in particular. Only by mid summer ($L_s \sim 110°$ in the north, $L_s \sim 290°$ in the south) does strong polar upwelling cease, allowing significant methane to accumulate here, having been advected in by the lower branch of the solsticial Hadley cell.

Surface methane evaporation is modeled according to Eq. (2). Fig. 6a shows the additional methane mole fraction required to saturate the lowest model layer (max[($Q_{sat} - Q_{CH4}$), 0]) while Fig. 6b shows the actual methane evaporation rate (Ev_{CH4}), averaged over 4 years of INF. The similar pattern demonstrates the dominance of the sub-saturation effect when surface methane availability

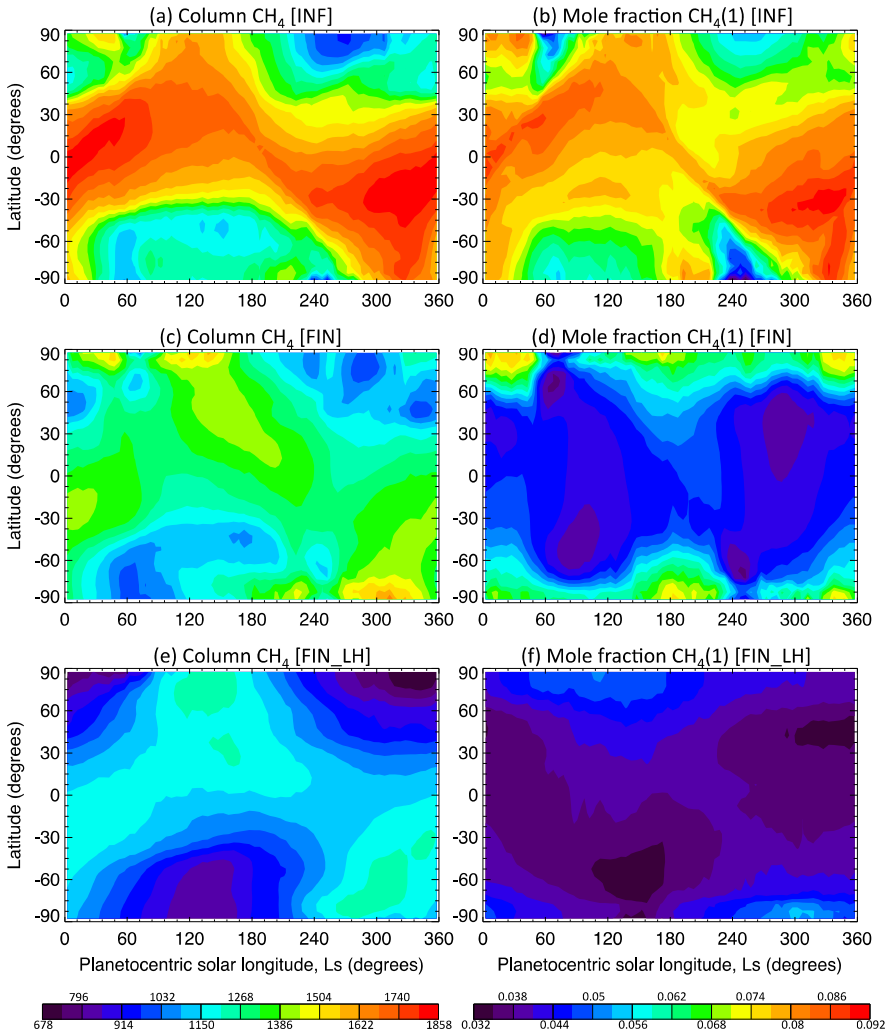

Fig. 5. Left column (a, c, and e): zonal mean column methane vapor (in kg m^{-2}). Right column (b, d, and f): zonal mean near-surface methane vapor mole fraction = (28/16) $q_{CH4}/(1 - q_{CH4})$, where q_{CH4} is the lowest layer methane mass mixing ratio in kg kg^{-1}. Results are shown as a function of latitude and L_s, averaged over the last four years of simulations (a and b) INF, (c and d) FIN, and (e and f) FIN_LH.

($Surf_{CH4}$) is not an issue. In spring/summer, warmer temperatures combined with the drop in high latitude near-surface methane due to strong upwelling (Fig. 5a) result in subsaturation of the near-surface and thus strong evaporation, peaking polewards of ~45° from $L_s \sim 50$–105° in the north and $L_s \sim 230$–285° in the south. Higher evaporation rates occur at southern high latitudes, due primarily to the warmer near-surface atmosphere during the shorter southern versus longer northern summer.

Fig. 7 shows zonal mean (a) surface evaporation; column-integrated (b) methane ice and (c) binary liquid condensation; (d) surface precipitation; and (e) evolving surface methane cover, for the last 3 years of INF, while Fig. 8 shows the vertical distribution of zonal mean methane ice condensate, binary condensate, and atmospheric re-evaporation for 4 Titan seasons. No pure liquid methane condensate is predicted in any simulation included here. We do not use the term 'cloud' because we do not include cloud microphysics but instead assume that condensed methane will reach the surface as precipitation unless it re-evaporates on the way down (see Section 2.2.1). However, these plots provide a proxy for where clouds might be expected. Fig. 7 shows significant repeatability from year to year. The pattern of methane condensation (Fig. 7b and c) is strongly correlated with the pattern of near-surface meridional convergence and upwelling shown in Fig. 4a and b, which respectively concentrates methane into the ITCZ and carries methane to higher layers (where lower temperatures produce saturation). The binary condensate is better correlated with the near-surface convergence, as it occurs at higher temperatures which occur closer to the surface and largely forms below 2–3 km (see middle column of Fig. 8). By contrast, methane ice condenses higher in the atmosphere (see left column of Fig. 8) where methane vapor is more well-mixed, and peaks where the greatest upwelling occurs. Ice condensation associated with the strong spring/summer polar upwelling can extend from the surface to 30 km around solstice, though generally peaks at ~6 km. Ice condensation related to the passage of the ITCZ shifts from the equator at equinox to summer high latitudes at solstice, sometimes extending nearly as high as the solsticial polar condensation, but mostly occurring much lower (below ~6 km) with smaller peak values (which also occur lower, at ~4 km).

Peak atmospheric re-evaporation (right column of Fig. 8) occurs in the lowest few km of the troposphere, below layers with large amounts of methane ice condensation. This indicates that the layers beneath the clouds are sub-saturated (most likely due to their methane having been lifted to higher levels by upwelling in the high latitude polar cells or in the ITCZ). However, re-evaporation typically extends down to the surface, indicating that – despite encountering sub-saturated layers – sufficient condensate remains by the lowest layer to produce precipitation, as shown in Fig. 7d for

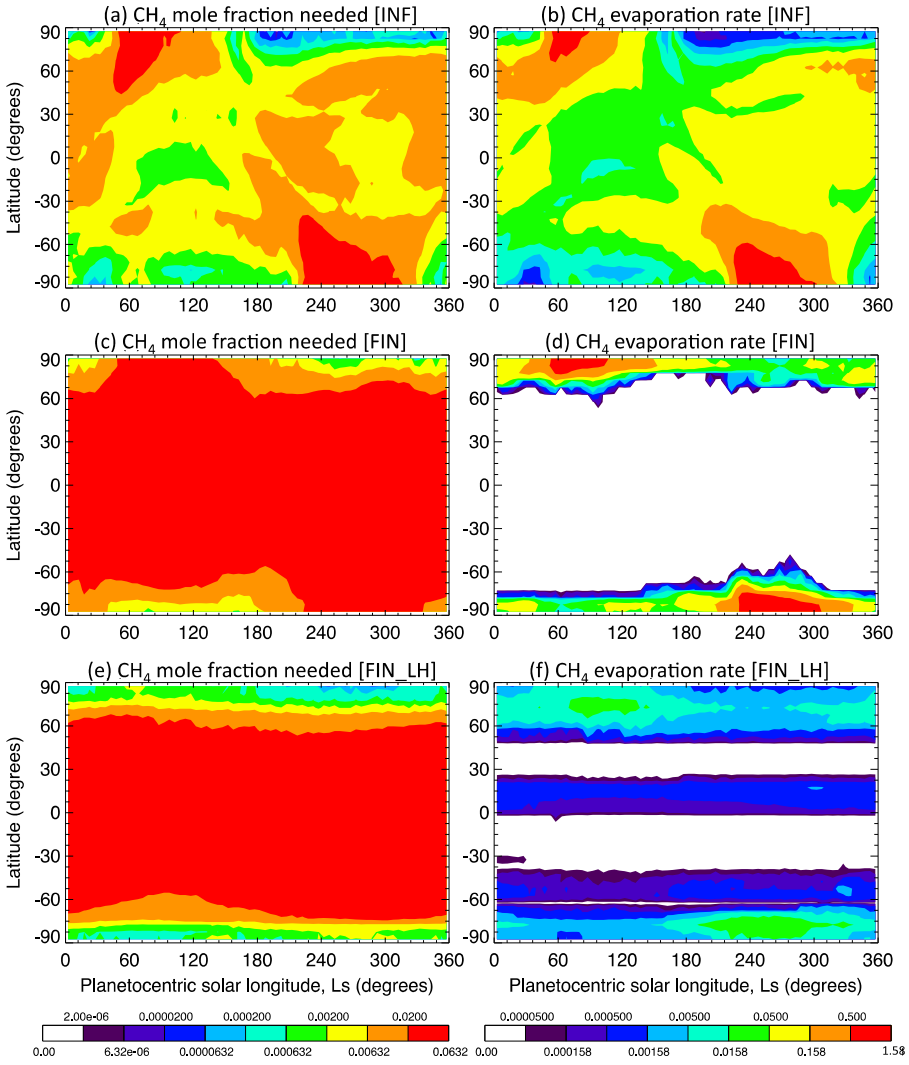

Fig. 6. Left column (a, c, and e): zonal mean additional methane mole fraction required to saturate the lowest model layer (term 'max[(Q_{sat} − Q_{CH4}), 0]' in Eq. (2)). Right column (b, d, and f): zonal mean surface methane evaporation rate in mm per Earth hour (LHS of Eq. (2), Ev_{CH4}). Results are shown as a function of latitude and L_s, averaged over the last four years of simulations (a and b) INF, (c and d) FIN, and (e and f) FIN_LH.

both condensate types combined. Comparison with Fig. 7b and c indicates that both ice and binary condensate influences the pattern of precipitation; while the largest amounts match the distribution of ice condensate, weaker precipitation is also produced by the lower-altitude binary clouds.

3.1.3. The passive methane cycle assuming finite surface methane (simulation FIN)

On Titan we see lakes only at high latitudes with relatively very dry low and mid latitude regions. Results from INF are thus unrealistic as they include an unphysically large source of methane at low and mid latitudes. However, INF does predict drying out of low and mid latitudes and wetting of high latitudes, with transfer of methane from lower to higher latitudes, as previously noted in axisymmetric simulations by Mitchell (2008) and in full simulations by Lora et al. (2014, 2015). Fig. 7e shows the change in surface methane cover, relative to the initial value, over the last 3 years of INF. Blue and purple colors indicate loss of methane (total evaporation exceeding total precipitation) at most low and mid latitudes (except for a band around 30°S and a narrower band around 30°N), with strong accumulation (total precipitation exceeding total evaporation) at latitudes poleward of ∼70° in both hemispheres. Fig. 9a shows the cumulative evaporation, precipitation, and change in surface methane at 87.5°N and S over the last 3 years of INF, and demonstrates the dominance of precipitation over evaporation at high latitudes, resulting in net gains in high latitude surface methane each year. These results suggest that if we had run simulation INF to a full steady state it would have produced a more Titan-like surface methane distribution naturally.

However, it would be hundreds more years before any surface grid points were exhausted in INF. We therefore sped up the process by initializing simulation FIN with a far smaller globally-uniform surface methane abundance of 5×10^3 kg m^{-2} (equivalent to ∼11 m depth), ensuring that exhaustion of surface grid points would begin in a few years. Lorenz et al. (2008) estimated 4×10^3 kg m^{-2} of methane in the atmosphere, 200–2×10^3 kg m^{-2} of ethane/methane in the lakes and an unknown amount of carbon in the likely porous or organics-covered surface, in which case 5×10^3 kg m^{-2} would be close to the lower limit capable of providing sufficient atmospheric methane to match that observed. FIN required ∼24 years to reach a full steady state and was then continued for another 21 years to be certain that no further long term changes would occur.

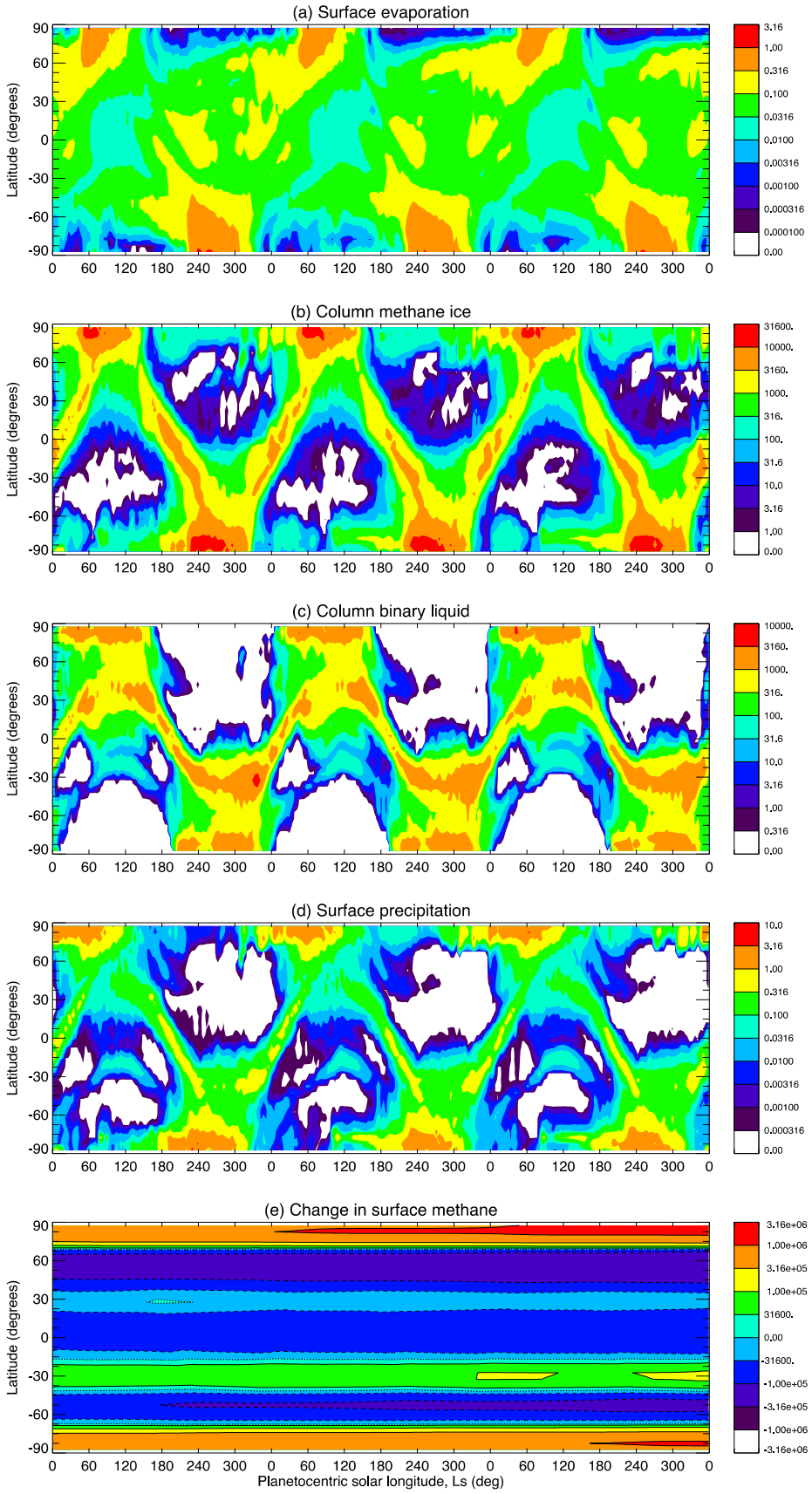

Fig. 7. Zonal mean (a) surface evaporation (in mm per Earth hour), (b) column-integrated mass of methane ice condensation in the troposphere (in kg m^{-2} over an 8 day period), (c) column-integrated mass of binary methane–nitrogen condensation in the troposphere (in kg m^{-2} over an 8 day period), (d) surface precipitation (in mm per Earth hour), and (e) difference between the surface methane depth (in mm) and its initial value of 2.22×10^5 mm, as a function of latitude and L_s for the last three years of simulation INF. Note the use of logarithmic contour intervals. In figure (e) solid [dashed] lines indicate contours of increased [decreased] surface methane cover, while dotted lines indicate locations with no change.

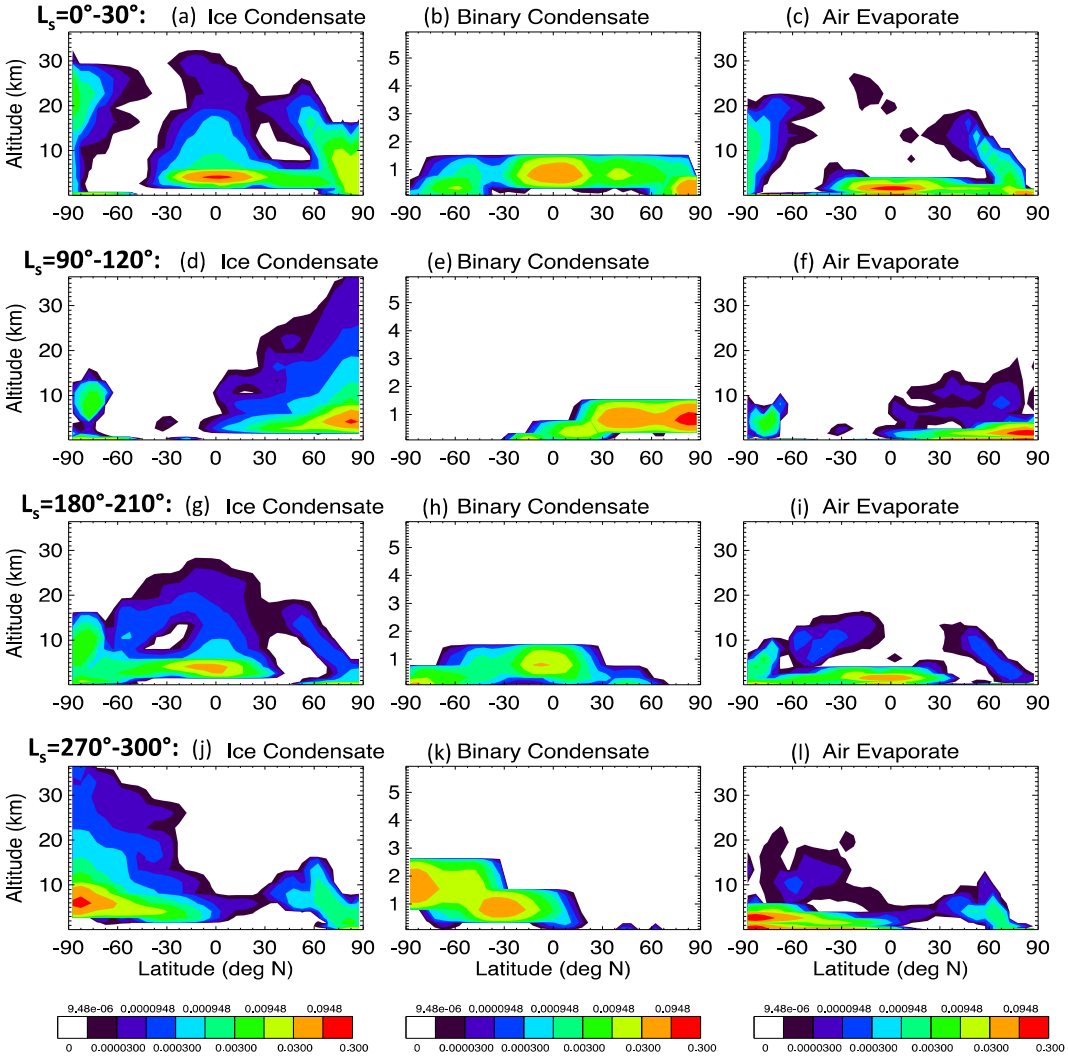

Fig. 8. Atmospheric condensation/re-evaporation as a function of latitude and altitude, averaged over the last four years of simulation INF in four time periods: (a) L_s = 0–30°, (b) 90–120°, (c) 180–210°, and (d) 270–300°. Left column: zonal mean methane ice condensate mass mixing ratio (in kg kg^{-1}). Middle column: zonal mean binary methane condensate mass mixing ratio (in kg kg^{-1}); note the reduced altitude range here. Right column: zonal mean atmospheric re-evaporation mass mixing ratio of both condensate types (in kg kg^{-1}).

Fig. 10a shows the variation in surface methane at low and high latitudes for all 45 years of FIN. In the first 3 years, surface methane is transferred from lower to higher latitudes in both hemispheres until the former regions are exhausted. For the remainder of FIN there is negligible change at lower latitudes, while at high latitudes each year consists of a rapid increase in surface methane due to strong precipitation in local spring, followed by a slower decrease due to evaporation through spring and summer. From years 3–24, surface methane is basically restricted poleward of ~70° (Fig. 11e). Although very weak precipitation can occur at slightly lower latitudes, it is rapidly re-evaporated (compare Fig. 11d and a) and does not show up in the surface methane plot. The high latitude surface methane is gradually rearranged via seasonal atmospheric transport, and the annual mean surface methane cover in these regions varies considerably from year to year (Fig. 10a). This 'adjustment period' occurs because the high latitude surface methane distribution that formed initially (when surface methane was available everywhere) is inconsistent with the net atmospheric transfer of methane later on (when low and mid latitudes are exhausted and the only source is at high latitudes in both hemispheres). From year 24 onwards, however, the annual mean surface methane cover does not change, and a steady state exists with ~50% more surface methane at northern than southern high latitudes. Note that surface methane rearrangement prior to the simulation reaching steady state is affected by year-to-year variability in the modeled methane cycle, but we have begun simulations at different seasons in different model years and find that – while surface methane evolution during the 'transient' period may vary – the steady state surface methane distribution is robust.

Fig. 9b further demonstrates the steady state nature of FIN by its end, showing evaporation, precipitation, and impact on surface methane cover at two high latitude grid points over the final 3 years. At both 87.5°N and 87.5°S, precipitation occurs faster than evaporation during the spring but the same total amount of both occurs each year, and consequently there is no net change in surface methane. Fig. 11e shows the zonal mean surface methane distribution over the final 3 years of FIN, and the year-to-year repeatability further supports the idea that FIN has reached steady state. Surface methane is present polewards of ~80° year-round, and also exists between ~70° and 80° following precipitation, which remains on the surface for up to half a year before re-evaporating.

A major feature of Fig. 11e is that the areal coverage is almost symmetric in both hemispheres; i.e., the 50% larger mass of surface

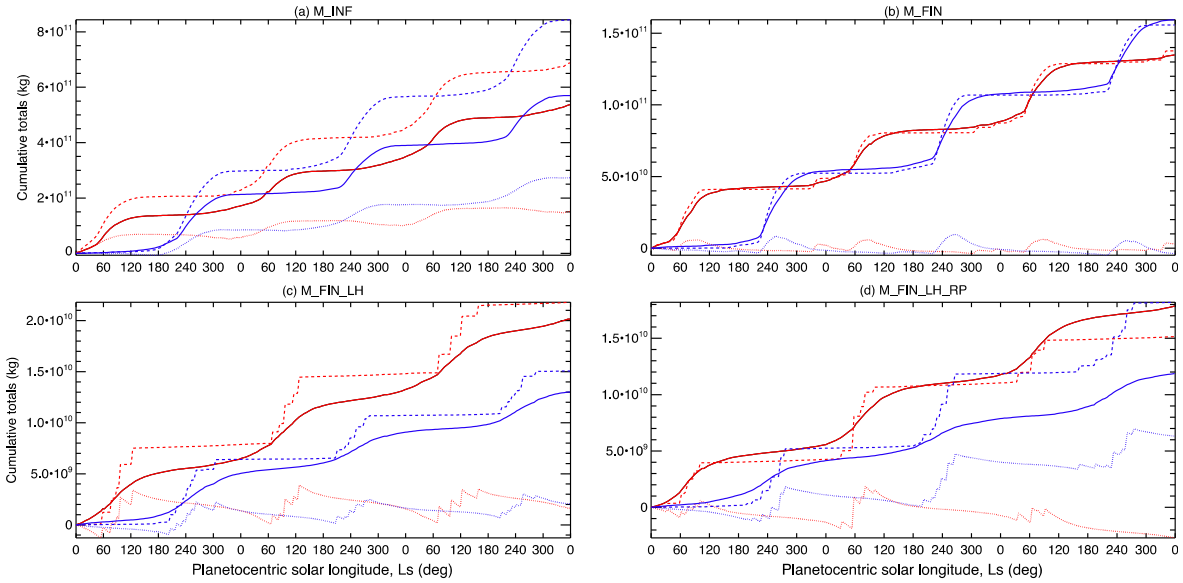

Fig. 9. Cumulative evaporation (solid lines), precipitation (dashed lines) and change in surface methane (dotted lines) in kg at 87.5°N (red lines) and 87.5°S (blue lines) as a function of L_s for the last three years of simulations (a) INF, (b) FIN, (c) FIN_LH, and (d) FIN_LH_RP. Note that FIN_LH_RP has not yet reached steady state, thus (d) shows a transient stage of the reversed perihelion simulation and should not be expected to mirror (c). (For interpretation of the references to color in this figure legend, the reader is referred to the web version of this article.)

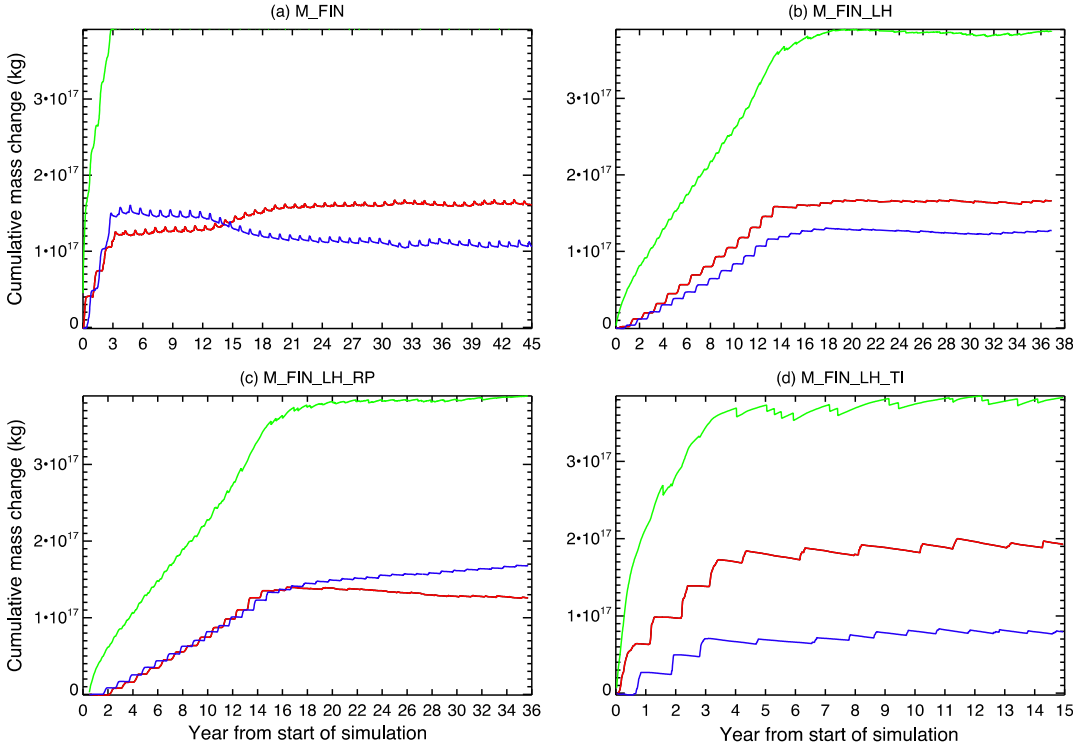

Fig. 10. Increase in surface methane mass (in kg) poleward of 70°N (red line) and poleward of 70°S (blue line), and decrease in surface methane mass (in kg) for all latitudes equatorward of 70° (green line), as a function of time for simulations (a) FIN, (b) FIN_LH, (c) FIN_LH_RP, and (d) FIN_LH_TI. (For interpretation of the references to color in this figure legend, the reader is referred to the web version of this article.)

methane in the north is largely due to a greater depth of methane on the surface rather than a greater area of surface methane coverage. The mechanism behind this, its relation to the active methane cycle results (Section 3.2), and how these results may relate to real Titan, are discussed further in Section 4.

The seasonal methane cycle in FIN is impacted by the lack of a low/mid latitude surface methane source. Comparing the FIN column methane abundances (Fig. 5c) with those for INF (Fig. 5a), we find that while peak values are up to 25% lower, particularly at low-latitudes, the distribution evolves rather similarly as a function of latitude and time. This is because the circulation redistributes methane so as to produce a similar pattern within the bulk atmosphere. Near-surface methane abundances (compare Fig. 5d and b) are slightly smaller at high latitudes, but seasonal variations are also rather similar to those in INF, with e.g. depletion during strong upwelling events in late spring/early summer. At low

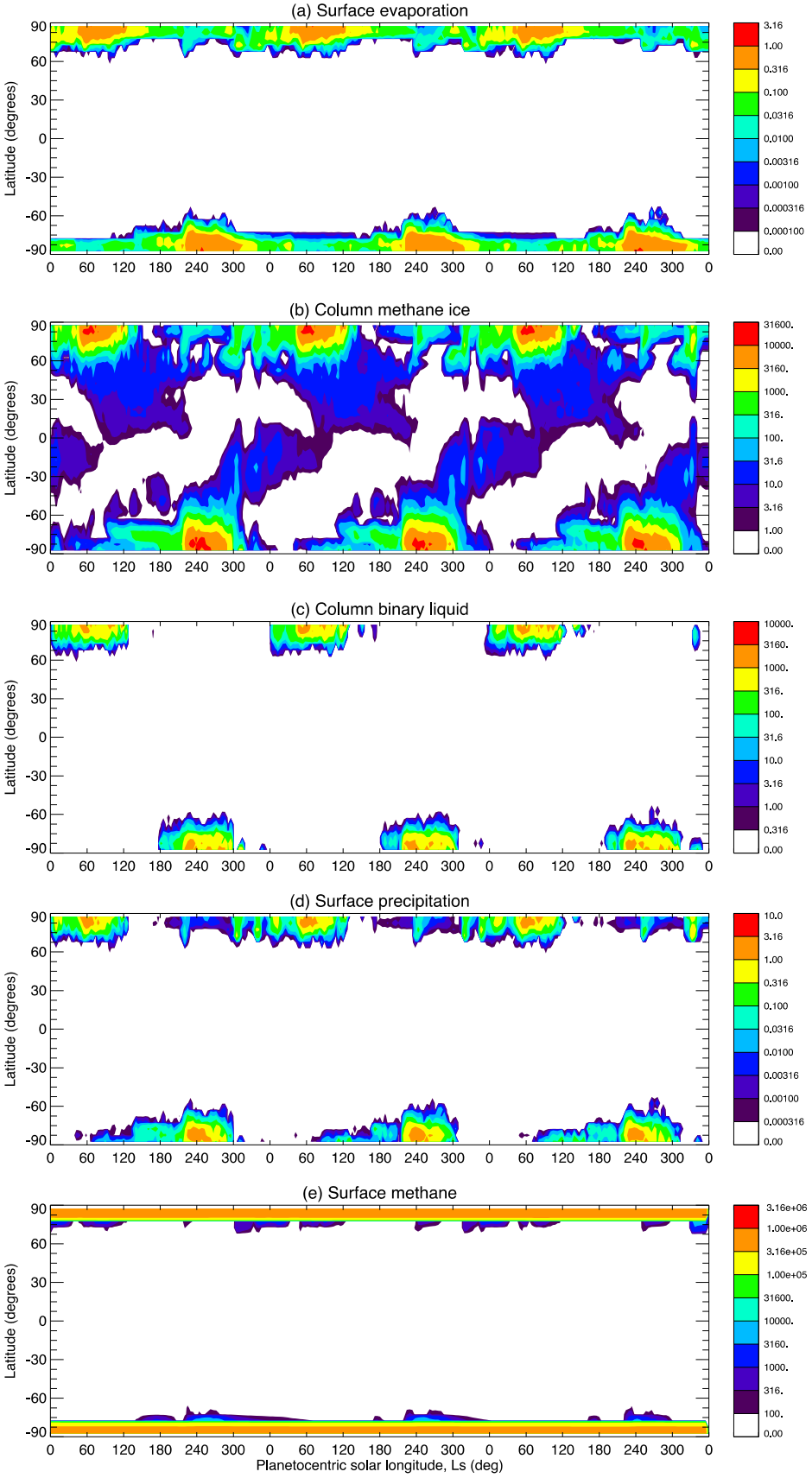

Fig. 11. Zonal mean (a) surface evaporation (in mm per Earth hour), (b) column-integrated mass of methane ice condensation in the troposphere (in kg m^{-2}), (c) column-integrated mass of binary methane–nitrogen condensation in the troposphere (in kg m^{-2}), (d) surface precipitation (in mm per Earth hour), and (e) surface methane depth (in mm), as a function of latitude and L_s for the last three years of simulation FIN. Note that (e) shows surface methane depth, rather than the change in surface methane abundance shown in Fig. 7e.

and mid latitudes, however, near-surface abundances are reduced by more than 50%, with little evidence of a peak following the location of ITCZ convergence since there is no surface source to be gathered into the ITCZ by the near-surface 'return flow' of the Hadley cells.

The lack of near-surface methane at low and mid latitudes means the lowest model layer is strongly sub-saturated here, as shown in Fig. 6c. This would result in strong evaporation if surface methane were available; however, the surface here is dry, thus the $Surf_{CH4}$ term dominates in Eq. (2) and produces the pattern of evaporation (restricted to high latitudes) shown in Fig. 6d (and over 3 years of FIN in Fig. 11a). This is similar to the pattern of high latitude evaporation in INF, peaking in late spring/early summer, though there is increased 'background' evaporation at other times of year too, due to sub-saturation caused by enhanced mixing of methane from the methane-rich high latitudes to the relatively methane-poor lower latitudes in FIN. Note that evaporation occurs when atmospheric mixing and transport (e.g. during a strong upwelling event) clears the near-surface of enough methane to sub-saturate it, rather than evaporation producing the pattern of near-surface methane. That is, a decrease in near-surface methane leads to enhanced evaporation, rather than an increase in evaporation leading to more methane in the near-surface layer. This is because the amount of methane removed by dynamic mixing is more than that supplied by evaporation – i.e., the dynamic timescale is shorter than the evaporation time scale in the passive methane simulations.

The pattern of condensation is also impacted by the smaller methane abundances overall, the greatly reduced abundances at low and mid latitudes, and the reduced signal of the seasonally-evolving ITCZ. At high latitudes the late spring/summer methane ice in FIN (Fig. 11b) is nearly identical to that in INF (Fig. 7b), with only a slight reduction in abundance of a few percent, while binary methane condensation is reduced by a factor of two or three (compare Figs. 7c and 11c). Equatorward of ~60°, however, ice production falls by up to two orders of magnitude, especially at lower altitudes (see Fig. 12, left column), and binary methane condensation is entirely suppressed. The impact on binary methane is greater because it forms at lower altitudes, thus is more sensitive to the availability of near-surface methane, whereas ice forms at higher altitudes where atmospheric transport of methane vapor mixes it more effectively over all latitudes and moderates the impact of the lost low and mid latitude surface source.

The huge reduction in low and mid latitude saturation and thus condensation results in no precipitation at these latitudes, as shown in Fig. 11d. Any condensate formed re-evaporates well before reaching the surface (see Fig. 12, right column). At high latitudes, peak precipitation is ~10% smaller than in INF, and long

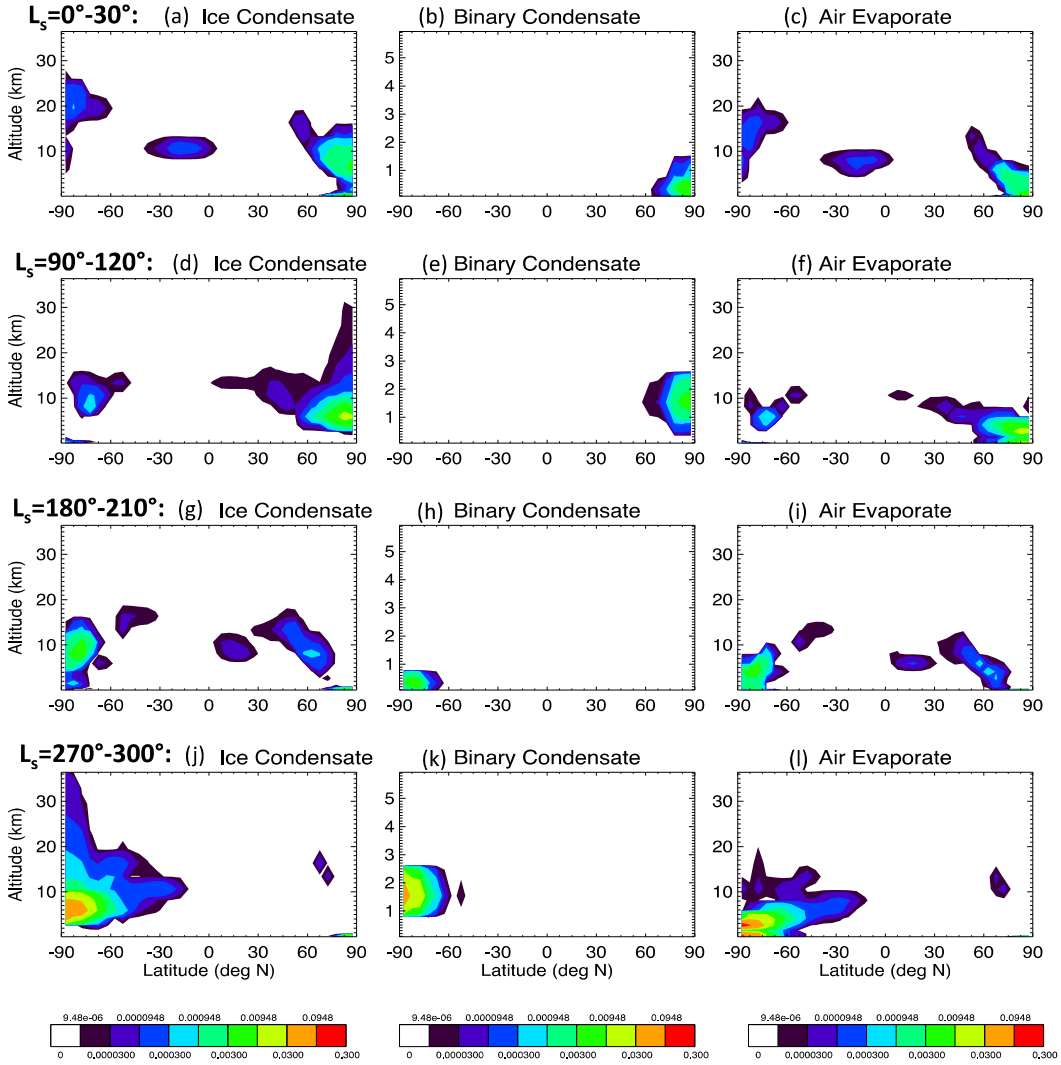

Fig. 12. Atmospheric ice condensation (left), binary condensation (middle), and re-evaporation (right) as a function of latitude and altitude at four times of year, as shown in Fig. 8 but now for simulation FIN.

gaps in precipitation occur around equinox, particularly in the south. As in INF, the pattern of precipitation is more correlated with the presence of ice, which – although produced higher up than binary condensation – is ~100 times stronger.

3.2. Active or 'moist' methane cycle results (simulation FIN_LH)

Section 3.1 described the methane cycle simulated without latent heating feedbacks (the passive or 'dry' case). Now we include the effect of surface evaporation and atmospheric evaporation/condensation on surface and air temperatures and the resulting circulation (the 'moist' case). Here, and in the remainder of this paper, we look at only 'finite methane' simulations – i.e., all are initialized with a low enough surface methane abundance (5×10^3 kg m^{-2}) that they reach a full steady state (with drying out of low/mid latitudes) in several years.

3.2.1. Variation of surface methane in FIN_LH

Fig. 10b shows the variation in surface methane over all 37 years of simulation FIN_LH, which has latent heating activated in the atmosphere and at the surface (see Section 2.2.3). As in passive simulation FIN, the steady state (year 18 onwards) surface methane distribution in FIN_LH consists of exhausted low and mid latitudes and accumulation at high latitudes. However, surface methane extends down to slightly lower latitudes in FIN_LH (at least ~70° in both hemispheres, versus ~80° in FIN; see Fig. 13d), and there are also occasional condensation events in low/mid latitudes (Fig. 13b) that are strong enough to produce precipitation (Fig. 13c) outside the high latitudes, resulting in transient low/mid latitude surface methane that re-evaporates over two or three years. But the biggest difference in FIN_LH is the nature of the hemispheric asymmetry, which now consists of both thicker methane deposits *and* greater areal coverage in the north, with surface methane extending from the pole to ~60° in the north, compared to ~70° in the south. The mechanism behind this, and difference to the behavior in FIN, is discussed in Section 4.

3.2.2. Thermal forcing and the circulation in FIN_LH

These differences in the steady state surface methane distribution are due to the altered thermal forcing, circulation and coupled methane cycle in the active simulation FIN_LH. Fig. 1c demonstrates that when evaporative cooling is included, surface temperatures are greatly reduced over areas with surface methane present (i.e., high latitudes). This produces far larger equator-to-pole temperature gradients, peak temperatures occurring near the equator at equinox rather than at the poles in summer, and a lower mean surface temperature overall. Although the biggest temperature reductions are in spring/summer, evaporative cooling also has an impact on high latitude surface temperatures in autumn/winter, as near-surface methane is slowly lost to the dry low and mid latitudes via down-gradient mixing and thus low levels of surface methane evaporation are needed to maintain saturation.

FIN_LH also has lower surface temperatures at low/mid latitudes, where very little methane evaporation occurs (Fig. 13a), indicating this is not due to evaporative cooling but rather to changes in the circulation and latitudinal heat transport. The altered thermal forcing in FIN_LH drives these circulation differences. Latent cooling of the polar atmosphere results in a large temperature gradient at ~60–70° latitude in both hemispheres, both at the surface and in the lowest ~5–10 km of the atmosphere (Fig. 1c and middle column of Fig. 14). This in turn affects the zonal wind, producing significant summer polar jets (right column of Fig. 14). By contrast, the atmosphere in passive simulation FIN (Fig. 3) is essentially isothermal across the tropics and into the higher summer latitudes, resulting in very weak zonal winds there. The restriction of the latitude range of peak thermal forcing from pole-to-pole in FIN to less than ~45° in FIN_LH (compare Fig. 1b and c), and the sharp thermal front at higher latitudes, reduces the latitudinal extent of the solsticial Hadley cells below ~5–10 km. This is reflected in the reduced latitudinal extent of the ITCZ, which moves between ~45°N and S over the course of the year in FIN_LH (Fig. 4c and d), rather than from nearly pole to pole in FIN (Fig. 4a and b). Peak vertical motion in the ITCZ and at the spring/summer pole merge in summer in the passive case (FIN, see Fig. 4a) – e.g., northern high latitude upwelling is part of a separate polar cell in Fig. 3a but merges with the global overturning cell in Fig. 3d. However, the systems remain completely separate in the active case (FIN_LH), yielding a double maxima in the summer vertical motion field (see Fig. 4c). These effects were first noted in the 'moist' simulation of Mitchell et al. (2006). The reduced spring/summer high latitude thermal forcing also results in weaker peak upwelling at high latitudes in FIN_LH than in FIN. However, upwelling is occasionally stronger than in FIN, at potentially any latitude, during intense condensation events.

3.2.3. Surface methane evaporation in FIN_LH

Two effects result in more than an order of magnitude less surface evaporation at high latitudes in FIN_LH compared to FIN (Fig. 13a): (i) when surface methane evaporation begins, evaporative cooling reduces surface and near-surface temperatures, thus reduces the amount of methane needed to produce saturation – i.e., there is a negative feedback effect that reduces evaporation; (ii) far weaker polar upwelling in spring/summer also removes evaporated methane far less rapidly from the high latitude near-surface, which prevents the late spring minima in near-surface methane seen in the passive simulations (compare Fig. 5b and d with f), and again results in less evaporation being required. These effects also act to smooth much of the near-surface methane variability; while near-surface methane abundance strongly affected the pattern of sub-saturation and hence evaporation for INF and FIN (compare e.g. Fig. 5b with Figs. 6a and b), temperature effects instead dominate the pattern of sub-saturation and hence evaporation for FIN_LH (compare Fig. 1c with Figs. 6e and f). This results in a gradual increase in high latitude evaporation through spring and a gradual decline through summer, linked to the seasonal evolution of surface temperatures. At low/mid latitudes, evaporation occurs only after transient surface methane has been deposited during strong condensation and precipitation events.

3.2.4. Methane condensation in FIN_LH

Fig. 13b shows the seasonal evolution of methane ice formation in FIN_LH. Peak condensation produces large releases of latent heat, and is thus associated with strong upwelling at high latitudes in local spring and summer. Other strong condensation follows the passage of the ITCZ between ~45°N and S (as shown in Fig. 4c and d), with low latitude condensation as it crosses from south to north around northern spring equinox favored over low latitude condensation around southern spring equinox. Background high latitude condensation occurs nearly year-round in the north, with larger gaps in the south during late autumn/early winter. The smaller evaporation rates and consequently smaller atmospheric methane abundances in FIN_LH result in the atmosphere never saturating with respect to binary condensation. Ice condensation is also reduced by as much as two orders of magnitude at high latitudes compared to FIN and consists of discreet events typically lasting between 10 and 30 days (Fig. 13b). The reduction in ice condensation and its 'patchier' nature are also due to the latent heat feedback in the active simulation: condensation results in latent heat release that warms the atmosphere, enabling it to hold more methane before becoming saturated, and thus reduces future condensation at the same level, tending

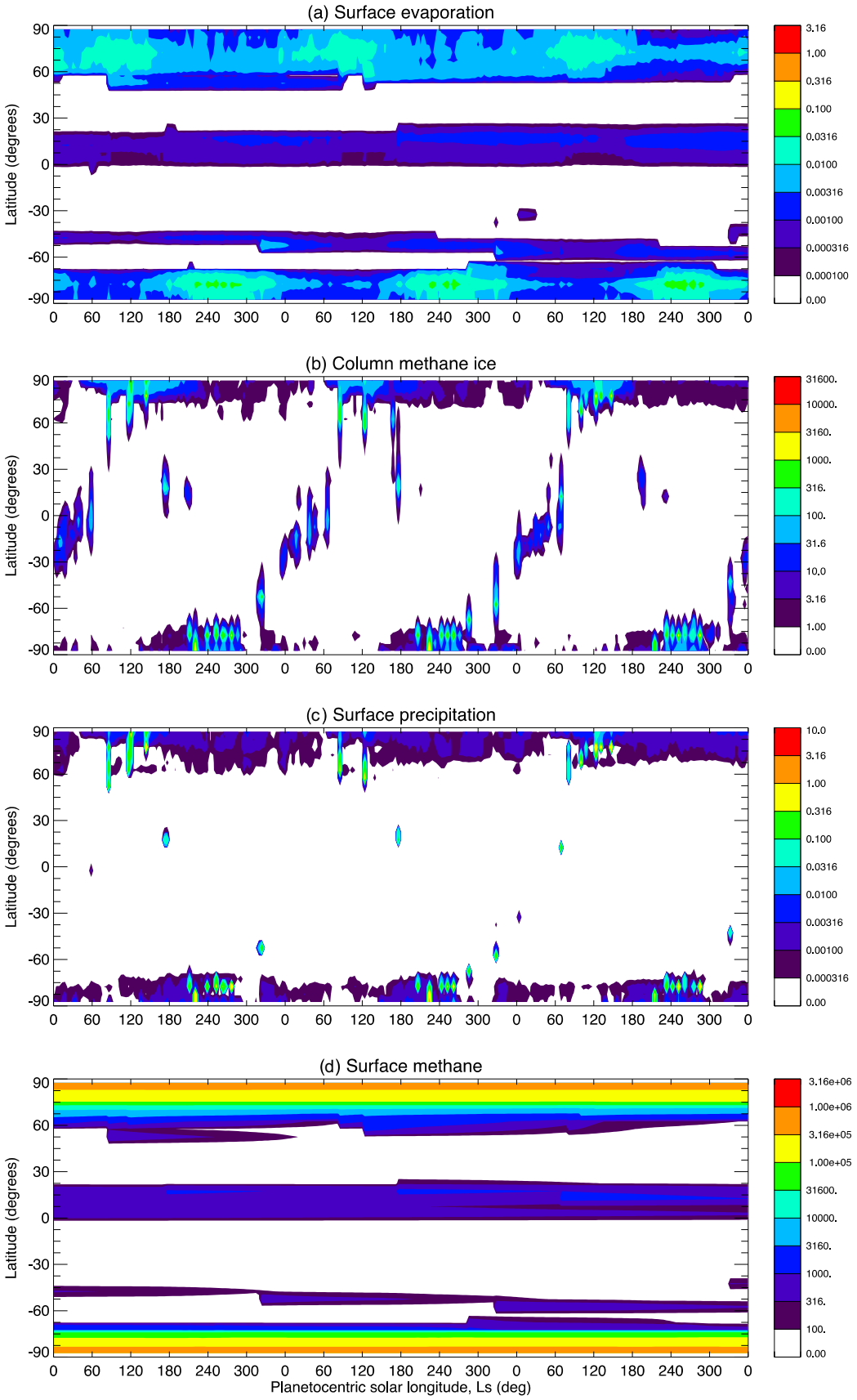

Fig. 13. Zonal mean (a) surface evaporation, (b) tropospheric column ice condensation, (c) surface precipitation and (d) surface methane depth, as shown in Fig. 11a, b, d and e, but now for simulation FIN_LH. Note that no binary methane condensation occurs in FIN_LH.

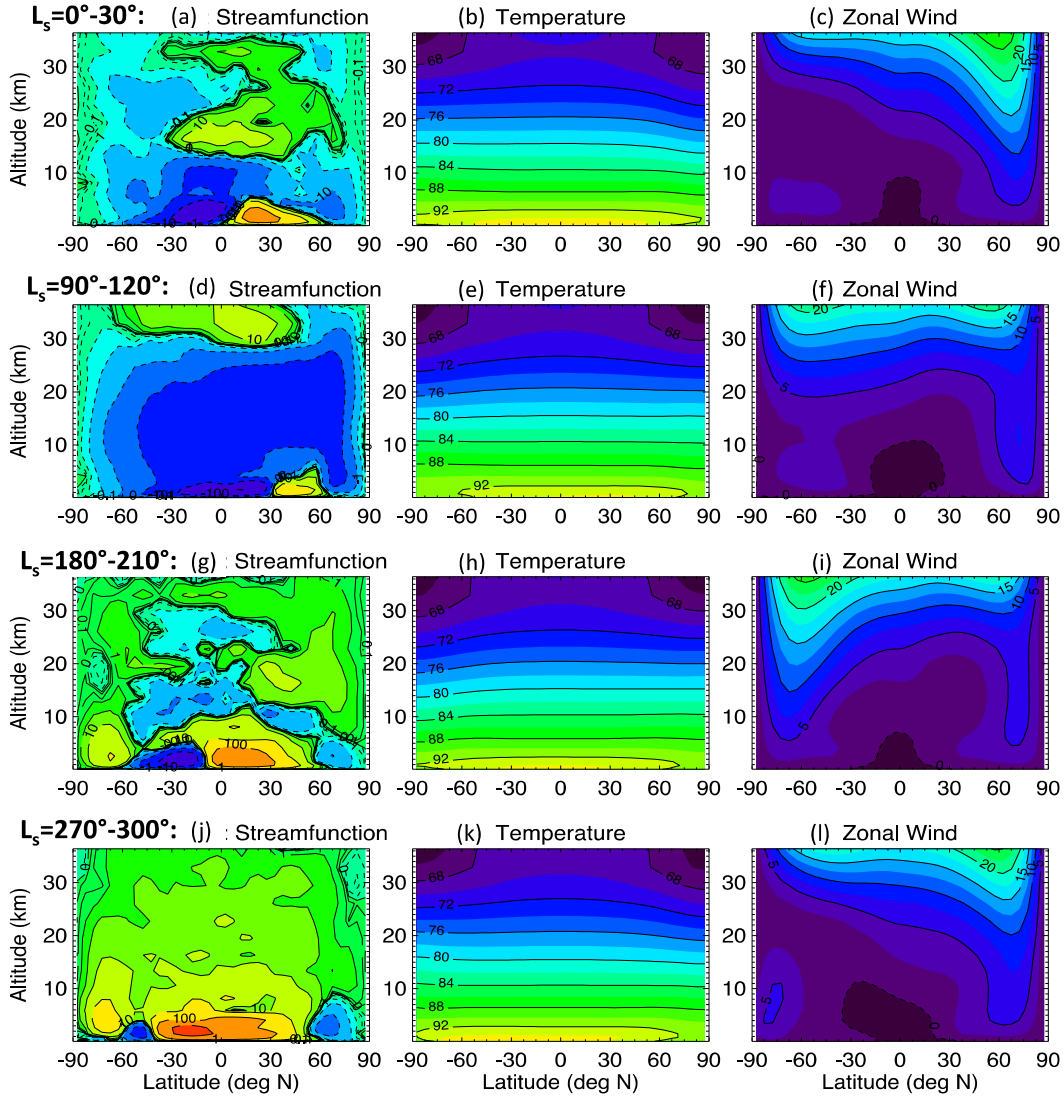

Fig. 14. The tropospheric circulation, as shown in Fig. 3 but now for active methane simulation FIN_LH.

to shut it down until either the atmosphere cools or more methane is transported in.

By contrast with the passive results (Figs. 8 and 12, left column), the height distribution of ice condensation for active simulation FIN_LH (Fig. 15, left column) is suggestive of Earth-like 'cumulus' convection. The largest condensation rates in FIN_LH are spread over a far more vertically-extended region from near the 'cloud base' to almost the 'cloud top' (which is as high as ~33 km at the poles in summer), rather than the bulk of the condensation being trapped below ~12 km in INF and FIN. This increased vertical extent is directly due to the release of latent heat which produces increased lift during the condensation process.

3.2.5. Methane precipitation in FIN_LH

Strong precipitation occurs for only the largest moist convective condensation events (compare Fig. 13b and c). Although most high latitude precipitation is one or two orders of magnitude smaller in FIN_LH than in FIN, it is much stronger during these events, which correlate with peak upwelling (see e.g. Fig. 4c). Unlike FIN (Fig. 11d), precipitation also occurs at mid and even occasionally at low latitudes in FIN_LH (Fig. 13c), again in the form of large moist convective condensation events, despite the lower zonal mean column methane abundances in the active simulation. Weak condensation occurs around both poles at very low altitudes over much of the year. This 'surface fog' is produced when near-surface sub-saturation results in surface evaporation, which cools the surface and rapidly cools the near-surface too (largely via sensible heat fluxes). This in turn produces saturation and condensation in the lowest layer that immediately falls out to the surface, hence its pattern is tightly linked to the 'background' precipitation in Fig. 13c.

3.2.6. Comparison of FIN_LH with observations of Titan's tropospheric circulation

Fig. 2 shows simulated surface temperatures at two times of the Titan year, compared with those observed by CIRS (Jennings et al., 2009, 2011). Whereas the surface temperatures in passive simulation FIN compare reasonably well with the observations, the evaporative cooling at high latitudes in active simulation FIN_LH and the impact on the circulation results in a lower mean surface temperature and an equator-to-pole surface temperature gradient ~2.5 K larger than observed. One possibility is that we are using an inappropriate surface thermal inertia, and that the lack of evaporative cooling compensated for this error in the passive case. Currently we do not allow surface type (e.g. dry or wet) to affect thermal inertia, and further

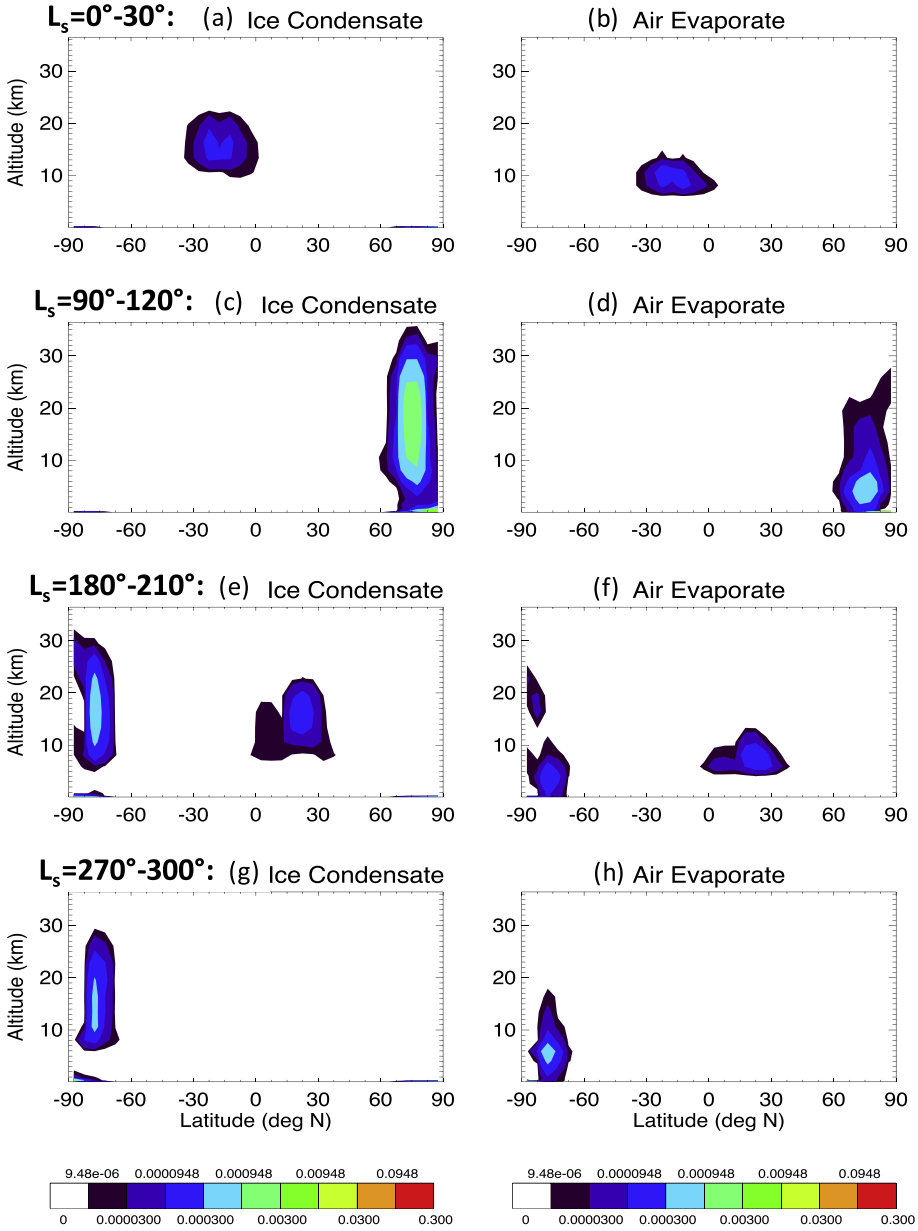

Fig. 15. Atmospheric ice condensation (left) and re-evaporation (right) as a function of latitude and altitude at four times of year, as in Fig. 8 but now for simulation FIN_LH (and with no middle column, since no binary methane condensation occurs in FIN_LH).

assume a globally-uniform value appropriate for a porous icy regolith (335 J m^2 $s^{-1/2}$ K^{-1}), which is toward the lower end of the range inferred from observations (Section 2.1.2). Liquid organics have a much higher specific heat capacity, hence would produce a much higher value of thermal inertia (~2.5 times greater). In Section 5 we show results from simulation FIN_LH_TI, which uses a higher value of thermal inertia, and demonstrate that this greatly improves the match to observed temperatures again.

Fig. 16a compares the temperature profiles observed by Huygens (Fulchignoni et al., 2005) with those simulated by INF or FIN and FIN_LH at the same location and time of year. In all cases the simulated temperature minimum is too sharp around the tropopause, the tropopause occurs several km too low, and the tropopause temperature is several degrees too cold. This likely indicates a need to re-calibrate and improve our radiative transfer calculations, which currently assume a pre-set methane distribution and a simple haze model (see Section 2.1.2), thus do not permit radiative feedbacks associated with the seasonally evolving methane or (more significantly) haze distribution. This is discussed further in Section 6.4.

Fig. 16b compares simulated and observed Huygens zonal winds (Bird et al., 2005). In the passive methane simulations (INF/FIN), zonal easterlies below ~10 km are slightly stronger than suggested by observations (though there is a gap in the observations between ~4 and 13 km), while zonal westerlies are much stronger than those observed above ~18 km. However, the predicted zonal winds are considerably weaker in the active methane simulation (FIN_LH), giving a much better match to observations. This may demonstrate the importance of the feedback on the tropospheric circulation when methane thermodynamics are included – which, as already noted in Section 3.2.1, serves to reduce the intensity of high latitude upwelling and generally weaken the circulation overall. In Section 3.2.9 we discuss the impact on the stratospheric circulation of the active methane cycle in FIN_LH.

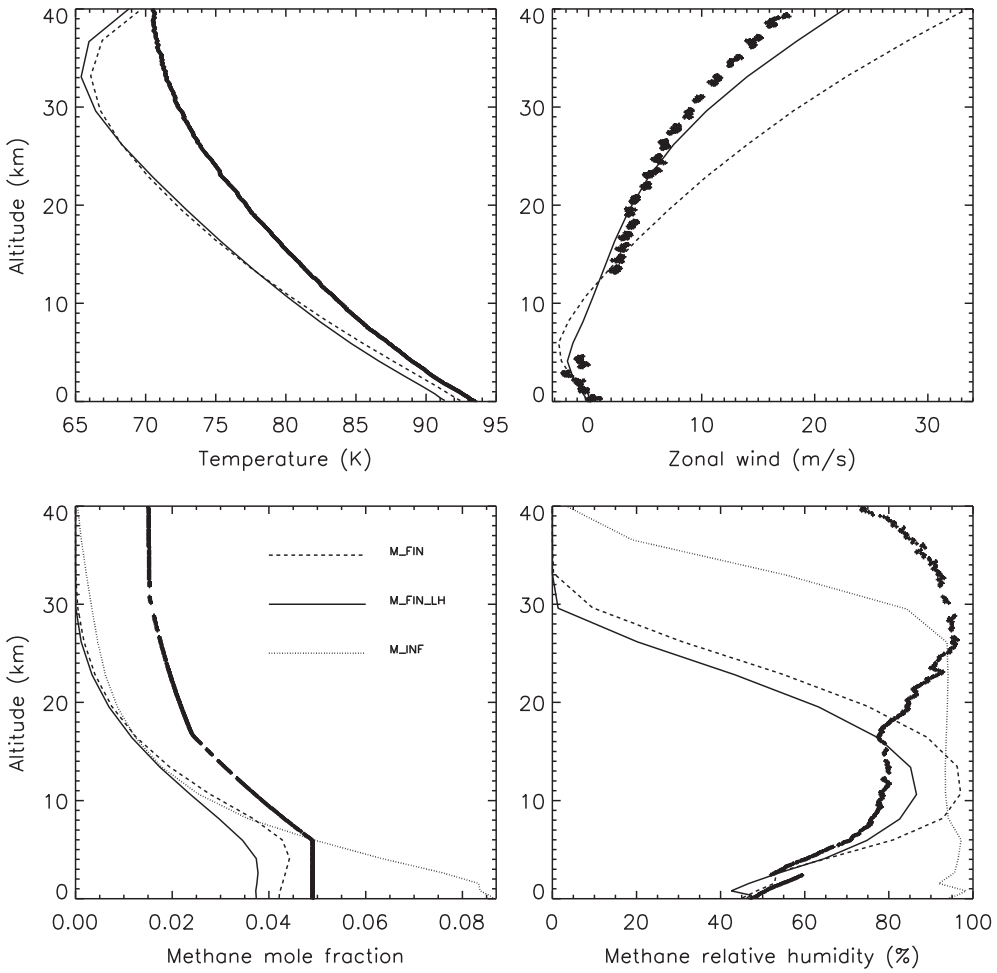

Fig. 16. Huygens data obtained during descent through the troposphere (plotted as symbols) and TitanWRF profiles for the Huygens entry latitude (10.2°S) and season (L_s = 300.5°) from simulations INF (dotted line), FIN (dashed line), and FIN_LH (solid line). (a) Zonal mean temperatures and Huygens Atmospheric Science Investigation (HASI) data (Fulchignoni et al., 2005). (b) Zonal mean zonal winds and Doppler Wind Experiment (DWE) data (Bird et al., 2005). (c) Zonal mean methane mole fractions and Huygens Gas Chromatograph Mass Spectrometer (GCMS) data (Niemann et al., 2005). (d) As in (c) but using temperatures and methane abundances to plot relative humidity profiles (see text for more details). Note that INF results for (a and b) are identical to those for FIN. Note also that saturation vapor pressures are calculated for both TitanWRF and Huygens using Eq. (1), thus the Huygens-derived relative humidities also ignore the lowering of the freezing point for binary methane condensation.

3.2.7. Comparison of FIN_LH with observations of Titan's tropospheric methane cycle

Fig. 16 also compares simulated and Huygens methane abundances (Niemann et al., 2005), in terms of both (c) methane mole fraction and (d) relative humidity. Due to its unlimited surface methane supply, simulation INF greatly overpredicts methane abundances in the lower half of the troposphere and differs greatly from the finite methane (FIN and FIN_LH) results, thus we focus on the finite simulations only. In terms of mole fraction, both FIN and FIN_LH underpredict the observed methane abundance by ~20–50% below 18 km, FIN_LH more so than FIN. In terms of relative humidity the match to observations below 18 km is better, due to the cooler-than-observed temperatures in both the passive and active simulations, which increases the relative humidity for the same mole fraction amount. Above 18 km, however, it is clear that both simulations greatly underpredict the observed methane abundances, with no methane remaining by ~40 km. This is in part due to the increasing cold bias with altitude, resulting in more condensation and removal of methane with height than in the real atmosphere, whereas in reality background and moist convective vertical motions would carry methane vapor and small condensed particles above this condensation level.

The pattern of ice condensation shown in Fig. 13b may be compared with the record of telescopic and Cassini cloud observations as summarized in e.g. Brown et al. (2010), Rodriguez et al. (2011) and Turtle et al. (2011a). Despite our use of only a large-scale condensation scheme and no complex parameterization of unresolved (sub-grid scale) moist convective processes, there are several areas of general agreement with observations. We predict south polar clouds to peak before $L_s \sim 300°$ (corresponding to January 2005), with less cloud activity from then until $L_s \sim 320°$ when intermittent clouds occur at high southern latitudes (~60°S). Following $L_s \sim 340°$ (January 2008), we predict that cloud activity should resume at mid-latitudes, moving steadily equatorward as we approach equinox, and moving into the northern hemisphere low latitudes some time between $L_s \sim 10°$ and 40° (~May 2010 and December 2012). The greatest disagreement is the absence of much predicted condensation in mid-latitudes (~35–55°S) between $L_s \sim 320°$ and 340°, despite several observations of clouds here at this time of year.

3.2.8. Comparison of FIN_LH with observations of Titan's surface methane distribution

In the absence of an LSM (see Section 2.2.2) we predict only whether a surface grid point is 'wet' (covered by methane) or 'dry' (methane-free), and assume a moisture availability of 50% where methane is present. We can therefore only compare with general observations of the 'wetness' or 'dryness' of different

regions of Titan's surface, and with estimates of the rate of loss or gain of surface moisture based upon observed changes in surface albedo and lake cover. The presence of dunes at low latitudes and lakes at high latitudes suggests that the former regions are relatively 'dry' (though Huygens measurements indicated methane adsorbed into the regolith at 10.2°S, Niemann et al. (2005)) and the latter regions relatively 'wet.' In addition, the far larger area covered by lakes in northern than southern high latitudes indicates a significant hemispheric asymmetry in surface methane abundance (Stofan et al., 2007). These observations are generally consistent with the results of FIN_LH. By the end of FIN_LH (Fig. 13d) methane has been largely removed from the low and mid latitude surface, while both hemispheres have permanent surface methane at high latitudes, extending down to ~70° in the south, and covering a larger area (down to ~60°) and with a greater depth in the north. The cause of this hemispheric asymmetry is discussed in Section 4.

Net loss rates (evaporation–precipitation) at southern high latitudes in late summer are ~0.02 mm/Earth hour (or ~0.18 m/Earth year) in FIN_LH, similar to those in the model of Schneider et al. (2012), and are the same order of magnitude, though smaller than, the lake loss rates inferred from the observed areal change in Ontario Lacus: ~1.0 ± 0.3 m/Earth year from June 2005 to July 2009 ($L_s \sim 306$–$359°$) (Hayes et al., 2011). Surface changes at ~80°S between July 2004 and June 2005 ($L_s \sim 293$–$306°$) have been used as evidence for rainfall (Turtle et al., 2009). This is immediately *after* the period of strong southern high latitude precipitation simulated in FIN_LH, although the last strong precipitation event occurs nearly this late in the season for the third simulation year shown (Fig. 13c). In addition to the high latitude permanent methane cover, transient methane coverage also occurs in FIN_LH between 60°S and 60°N, due to occasional precipitation events (each affecting only a few longitudes) which occur largely during the passage of the ITCZ through mid- and low-latitudes during late local summer and early autumn. This is consistent with other numerical models (Mitchell, 2008; Lora et al., 2015). Low-latitude rainfall was inferred at ~20°S in October 2010 ($L_s \sim 15°$; Turtle et al. (2011a, 2011c)) and while no precipitation is simulated at exactly this time and location in FIN_LH (Fig. 13c), other precipitation events are simulated at comparable latitudes as the ITCZ passes through. Given the low frequency of these events, more simulation years (and also more years of observations) are needed to gather better statistics, and make it possible to compare the predicted and observed spatio-temporal distribution of precipitation events.

3.2.9. Impact on the stratospheric circulation of an active tropospheric methane cycle

TitanWRF is not only a tropospheric model but also resolves the stratosphere and lower mesosphere up to ~400 km, and shows good agreement with the observed large magnitudes and general pattern of stratospheric superrotation (Newman et al., 2011). Fig. 17 shows the impact of our active methane cycle on the stratospheric circulation in terms of the zonal mean temperature and zonal winds at a time of year observed by CIRS, the period Ls ~ 293–323° (Achterberg et al., 2008). Note that the passive results

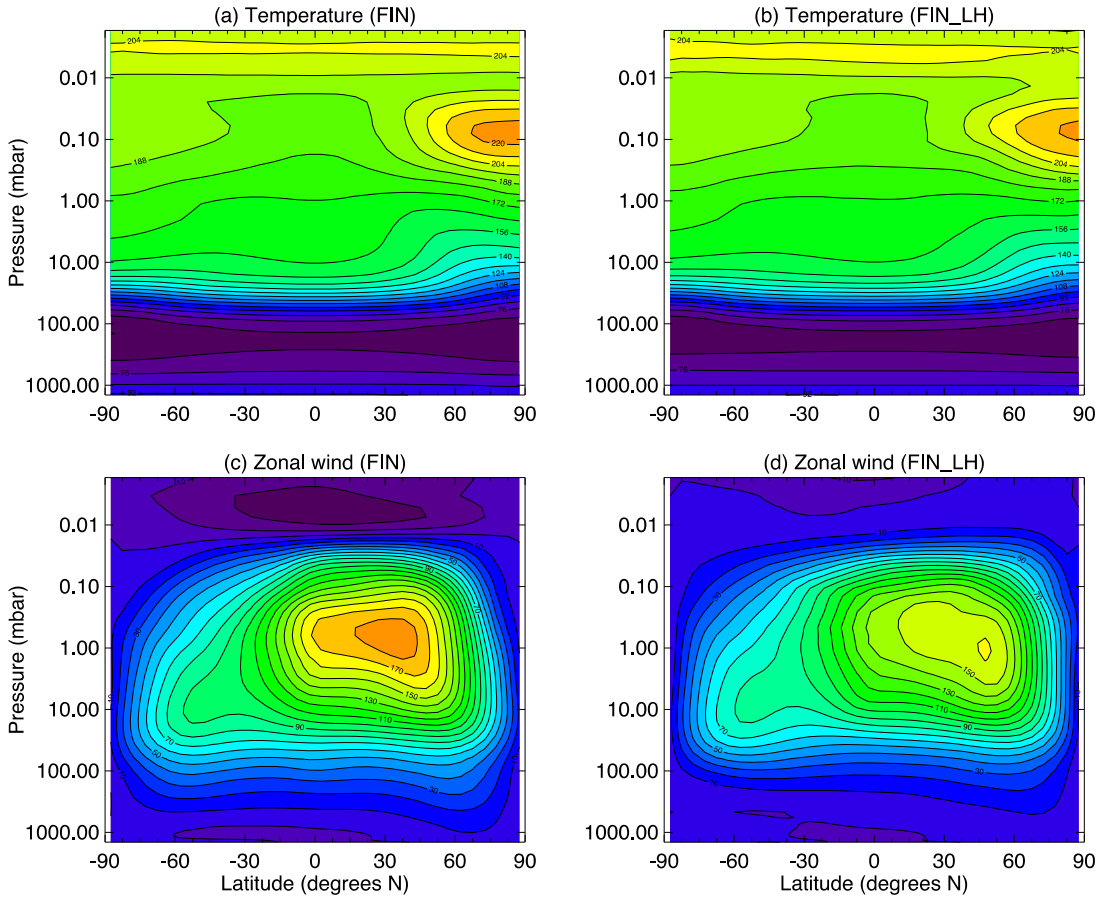

Fig. 17. Zonal mean temperatures (top row) and zonal winds (bottom row) from the surface through the stratosphere (0 to ~400 km), from passive methane simulation FIN (left column) and active methane simulation FIN_LH (right column), for the period $L_s \sim 293$–$323°$. The passive model set-up and hence results are identical to those in the lower right hand corner of Figs. 1 and 2 of Newman et al. (2011) (aside from tiny differences associated with year-to-year variability), which also showed CIRS observations for the same period.

are basically identical to those shown in Newman et al. (2011), as expected because the same model set-up is used here, with the only slight differences being a result of showing a different simulation year. With an active tropospheric methane cycle, the peak zonal winds are weakened by ~12% relative to the passive case, making them slightly less realistic. However, reduced zonal wind speeds in the lower stratosphere, with a stronger gradient in wind speed above them, is more consistent with observations.

The ability to simulate the methane cycle within a full troposphere + stratosphere GCM is useful, as the greater availability of observations related to the stratospheric circulation (e.g., temperatures and inferred zonal winds from CIRS) provides an additional way of constraining and validating our results. In fact, the results shown in this paper already benefit from what we learned when attempting to produce realistic superrotation in TitanWRF. As detailed in Newman et al. (2011), we found that there was too much horizontal diffusion imposed in the GCM and that this had an adverse impact on wave-mean flow interactions. All methane cycle simulations shown here were conducted with far less horizontal diffusion (see Section 2.1.1), but Fig. 4e and f shows the pattern of peak tropospheric upwelling and meridional divergence produced in a passive simulation with the 'old' diffusion used, and can be compared with the 'new' passive results in Fig. 4a and b. There are considerable differences, including weaker polar cells and stronger ITCZ upwelling in the 'old' diffusion case, which would certainly have impacted the methane cycle produced.

4. Investigating the cause of the hemispheric asymmetry in surface methane

FIN and FIN_LH both produce more surface methane accumulation at northern versus southern high latitudes. To verify that this asymmetry is due to the asymmetry in solar forcing, and to rule out the possibility of a systematic error in the model (e.g. a transport bias toward the north), we first demonstrate that it reverses when the solar forcing is also reversed (Section 4.1). We then describe the mechanism responsible for the hemispheric asymmetry in TitanWRF (Section 4.2) and compare our findings to previous results (Section 4.3).

4.1. Results of simulations with perihelion during northern summer

The current hemispheric asymmetry in solar forcing, used in simulation FIN_LH, consists of perihelion shortly after southern summer solstice at $L_s = 279°$, producing a shorter, warmer southern summer and a longer, cooler northern summer. Simulation FIN_LH_RP is identical to FIN_LH, except that perihelion occurs shortly after northern summer solstice instead at $L_s = 99°$. FIN_LH_RP is initialized from the end of a passive methane simulation that has been spun up to steady state using the 'reversed perihelion' orbital settings.

Fig. 9d shows the cumulative evaporation, precipitation and surface methane cover at 87.5°N and S over the last 3 years of FIN_LH_RP, while Fig. 10c shows the simulated variation in polar and equatorial surface methane for all 36 years of the simulation. Both demonstrate that FIN_LH_RP has not yet reached steady state. By contrast with the previous finite methane results shown in Fig. 9b (FIN) and c (FIN_LH), in which the cumulative surface methane at both high-latitude points oscillates approximately around zero, in Fig. 9d the surface methane at 87.5°N shows a small overall trend of decreasing with time, while that at 87.5°S shows a large overall trend of increasing. Similarly, the polar surface methane abundances in Fig. 10c still show long-term variation with increasing south polar surface methane by the end of FIN_LH_RP, indicating continuing exchange between the poles. Despite FIN_LH_RP not having quite achieved steady state, the build-up of methane in the south and the remaining trends suggest that the final surface methane distribution will be approximately a reflection about the equator of that in simulation FIN_LH, with more southern than northern high latitude surface methane by the time steady state is reached.

4.2. Cause of the hemispheric asymmetry in surface methane produced by TitanWRF

We suggest that the mechanism behind the hemispheric asymmetry in TitanWRF is as follows: Summer high-latitude near-surface temperatures are significantly warmer during the perihelion (currently southern) summer, when Titan is closer to the Sun, than during aphelion (currently northern) summer. Because of this, on average more methane can be held in the summer high-latitude atmosphere during perihelion summer than during aphelion summer; although perihelion summer is shorter, the non-linear relationship between temperature and saturation vapor pressure more than compensates for this. Regardless of the meridional circulation, the resultant gradient in atmospheric methane abundance from pole to pole (see e.g. the meridional gradients in column abundances shown in Fig. 5) is sufficient to produce net transport out of the perihelion summer (currently southern) high latitudes each year. Over the course of many years, this mechanism results in the depletion of surface methane in the south, and the accumulation of surface methane in the north (Fig. 10a, b and d), with the reverse happening when the timing of perihelion is reversed (Fig. 10c). The relative vigor of the transport circulation during the two solsticial seasons will qualitatively affect the rates of pole to pole transport, but as demonstrated in Figs. 5 and 10, does not reverse the down-gradient transport. As an aside, it is frequently noted that up-gradient water vapor transport is an observed feature of the terrestrial Hadley circulation (and locally, up-gradient methane transport occurs in the Titan WRF simulations) and thus reversal of the down-gradient transport on annual average time scales for the global budget may seem plausible at first glace. However, it should be noted that these non-intuitive residual features in the terrestrial atmospheric water transport are only possible because the total water transport on the Earth unavoidably also includes the vast amounts of water transported within the ocean (i.e. the transport that allows the vast differences of evaporation and precipitation between the tropics and extra tropics).

Our suggested mechanism is demonstrated by Fig. 9d, which shows the evaporation and precipitation at 87.5°N and S over several years prior to simulation FIN_LH_RP reaching steady state. While the late spring/early summer evaporation minus precipitation at the north pole is typically greater than zero, this situation is reversed at the south pole, producing a net surface methane loss in the north and gain in the south over the three years shown. Since the atmospheric column methane does not increase (not shown), evaporation exceeding precipitation in a given region each year must be associated with net annual transport of evaporated methane away from that region, and vice versa. By contrast, once a simulation has reached steady state - the situation shown for FIN and FIN_LH in Fig. 9b and c, respectively - evaporation and precipitation approximately 'track' each other at both the north and south poles.

4.2.1. What determines the steady state methane distribution?

While the mechanism described above explains why we might expect (for the present day) net transport from southern to northern high latitudes, it does not explain why such net transport would cease before the southern high latitude surface is exhausted of methane. I.e., it does not explain the steady state high latitude

methane distributions shown in Figs. 7e and 13d for simulations FIN and FIN_LH. Steady state occurs when a balance exists between north–south transport (largest during northern spring/summer) and south–north transport (largest during southern spring/summer). The question is, what produces this balance?

Provided it is deep enough that surface methane isn't exhausted, the *depth* of accumulated surface methane has no impact on evaporation rates in our simulations (we do not include its impact on thermal inertia, sub-surface heat transfer, etc.). Thus the only factor that can be relevant is the *areal* coverage of surface methane. The simplest explanation is that net transport from the southern to northern high latitude regions continues until the relative area of surface methane in the south is sufficiently less than in the north that this offsets the mechanism described above. I.e., in the steady state, the reduced source area available for evaporation in the south compensates for the greater intensity of net southern summer evaporation, resulting in slightly weaker pole-to-equator atmospheric methane gradients, and producing total transport away from southern high latitudes that exactly balances the amount transported away from the north in their respective summers.

This would explain the results of active simulation FIN_LH. Fig. 13d demonstrates the larger zonal mean surface area covered by methane in the northern hemisphere, which results in a larger zonal mean surface area over which evaporation occurs (Fig. 13a). Fig. 18 shows the fraction of a year for which each surface gridpoint in FIN_LH is covered with (c) any methane and (d) more than 100 mm of methane, and confirms that more surface area is covered permanently (time fraction = 1, in red) in the north than in the south.

This simple picture assumes a consistency of the transport efficiency over the course of the year, which is not the case. If the transport efficiency were the same during the two solstices, the strength of the asymmetry in the pumping of methane from pole to pole would be determined entirely by the relative durations of the solsticial seasons (i.e. to the eccentricity of the orbit and the argument of perihelion) and by the area of the source, as suggested. In reality, the relative efficiency of the circulation in the two solstices will modify the 'balance point' between the methane source strength (thermal control), the source area, and the relative duration of the solstices. Determining the relative contribution of all of these terms, including transport efficiency, is beyond the scope of this paper. It is certainly not something that can be determined from simple examination of methane or energy fluxes, and is extremely hard to determine due to the integration of methane with the energetics moderating the atmospheric circulation. Note also that, by definition, there is no asymmetry in the total annual flux of methane between hemispheres *in the steady state model*, thus any investigation of the cause of the surface asymmetry must be conducted while the simulation is still 'spinning up' and the surface asymmetry is still developing.

The situation for passive methane simulation FIN is more complex. As shown in Fig. 11e, the surface area covered by methane in a zonal mean sense is the same in the north and south, and the region with permanent methane cover >100 mm (Fig. 18b) is also the same in both hemispheres. However, the region with any amount of permanent methane cover (Fig. 18a) is very slightly larger in the north than in the south, and the north also shows a region from 45 to 65°N that has some methane present for 70–85% of the year, compared to the same latitude range in the southern hemisphere where methane is present for only 60–75% of the year. While the FIN results are more marginal, they still support the general idea of an asymmetry in northern versus southern hemisphere surface methane reservoirs.

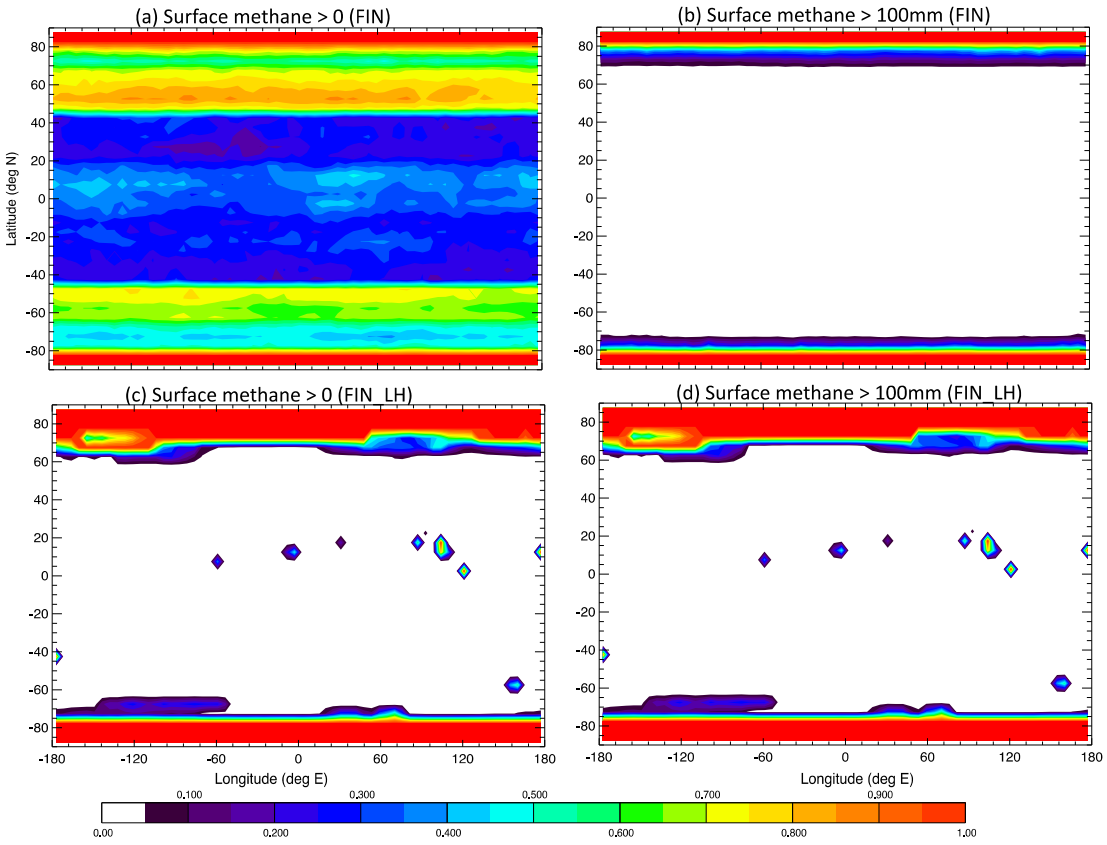

Fig. 18. Fraction of the year for which each surface grid point is covered by a depth of methane greater than 0 (left column) or 100 mm (right column), averaged over the last 4 years of simulations FIN (top row) and FIN_LH (bottom row). Red shading indicates fractional coverage = 1 (i.e. permanent methane coverage) of the given depth (0 or 100 mm). (For interpretation of the references to color in this figure legend, the reader is referred to the web version of this article.)

4.2.2. Why do the passive and active results differ?

The fundamental driver of the asymmetry suggested above – more net surface methane lost from high summer latitudes during the more intense southern summer – is present regardless of whether latent heating effects are turned on or not. However, as described in Section 3.2.2, latent heating feedbacks impact the entire methane cycle, from surface evaporation rates to the circulation pattern to the distribution of condensation and precipitation, all of which must affect seasonal south–north and north–south transport. As one example, note that in FIN (Fig. 9b) net polar accumulation occurs between mid spring and summer solstice (e.g., northern surface methane accumulates between $L_s \sim 50°$ and 90°, southern between $L_s \sim 230°$ and 270°). By contrast, in FIN_LH (Fig. 9c) the period of net polar accumulation is longer in both hemispheres, and also begins much earlier in the south ($L_s \sim 200°$) than in the north ($L_s \sim 60°$) relative to the start of spring ($L_s \sim 180°$ in the south and 0° in the north).

4.3. Comparison with the hemispheric asymmetry predicted by other models

Schneider et al. (2012) describe the results of their model, which included a hypothesized surface (or sub-surface) transport of methane from the poles to mid latitudes. They note that this was required to "maintain a statistically steady state with non-zero net precipitation in polar regions and asymmetries between the hemispheres." As described above, we did not find surface/sub-surface transport to be necessary to produce hemispheric asymmetry in high latitude methane abundance at steady state. This suggests that TitanWRF may allow more atmospheric transport of methane out of the polar regions on a seasonal basis than the Schneider et al. model, and thus not require such a 'resupply term.' It is likely that the circulation simulated in TitanWRF is rather different to that of the Schneider model, given that TitanWRF resolves the stratosphere up to ~400 km and produces strong stratospheric superrotation, which also affects the tropospheric circulation, whereas Schneider et al.'s model resolves the troposphere only, with no strongly superrotating atmosphere aloft. However, it is unclear how the Schneider et al. results differed prior to their addition of the resupply term; specifically, whether it was added in order to achieve a steady state solution, or simply to improve the match to observations. We discuss this further in Section 6.2.

In FIN_LH, polar temperatures are several K lower – and the equator-to-pole temperature gradient a few K larger – than those observed by CIRS, which will impact the steady state reached. In Section 5 we show results from simulation FIN_LH_TI, which uses a higher surface thermal inertia and predicts more realistic surface temperatures. This simulation predicts a larger hemispheric asymmetry in surface methane while continuing to predict reasonable amounts of cloud and precipitation at steady state with no surface or sub-surface transport required. In addition, the simulations of Lora et al. (2015) have surface temperatures similar to those observed, and as in TitanWRF produce a slight build-up of surface methane in northern versus southern high latitudes via atmospheric transport only.

5. Effect of increasing the surface thermal inertia

In the results shown above, TI was set to be globally-uniform and equal to 335 J m^2 s$^{-1/2}$ K^{-1}. Ideally, TI would vary spatially as inferred from observations of the surface, but Titan's thick atmosphere and the nature of Cassini's flyby observations make such measurements difficult to obtain. CIRS measurements of diurnal temperature variations near Titan's equator imply a rather large range of TI = 300–600 J m^2 s$^{-1/2}$ K^{-1}, though this still may not be representative of other regions (Cottini et al., 2012). As discussed in Section 3.2.2, the strong high latitude evaporative cooling in FIN_LH produces (i) overly-large meridional gradients in surface temperature, and (ii) mean and minimum surface temperatures several K too low, by comparison with observations. TI reflects the ability of the surface to store and conduct away heat, which determines how quickly it heats and cools, and is defined as TI = $(\rho_{surf} c_p{}^{surf} \kappa)^{1/2}$ (see Section 2.1.2). c_p is the amount of heat required to change a material's temperature, thus high $c_p{}^{surf}$ implies relatively slow daytime warming and nighttime cooling of the surface. κ is the rate at which heat is transferred through a material with an imposed temperature gradient, thus high κ implies that as the surface is heated and warms during the day this heat is transferred more rapidly into the sub-surface, slowing the rate of warming. Similarly, heat is returned more rapidly to the surface at night as the surface cools, slowing the rate of cooling. A higher value of surface thermal inertia should thus act to slow ('buffer') the evaporative cooling effect, resulting in weaker latitudinal temperature gradients.

Here, we examine the impact of using a globally-uniform TI = 2711 J m^2 s$^{-1/2}$ K^{-1}. This is well above the range determined from CIRS measurements, thus represents an extreme case as we begin to explore parameter space. ρ_{surf} and $c_p{}^{surf}$ were held constant, hence this TI value effectively increased κ to >6 W m^{-1} K^{-1}, an extremely high value that would likely not exist in Titan's subsurface. Simulation FIN_LH_TI is otherwise initialized exactly as in FIN_LH, and then run for 12 years until a steady state in surface methane is achieved, followed by another 3 years to produce the results shown. Fig. 1d shows the annual cycle of surface and near-surface temperatures averaged over the last 3 years of FIN_LH_TI. As expected, the impact of the increased surface TI is to reduce the latitudinal temperature gradients and to reduce the seasonal variation in temperatures near the poles. The global-mean surface temperature also increases, as expected for a higher TI. However, since increased TI manifests as increased thermal conductivity and we have not increased the depth of the model's subsurface, it is possible that some fraction of the increase is due to unphysically-fast contact with the fixed deep sub-surface temperature of 94 K (see Section 2.1.2). More work is needed to verify that this is not a concern, and to identify the most appropriate depth of the sub-surface model – and value of TI – for use in TitanWRF.

Fig. 19a, b and c shows the impact of the new atmospheric state on predicted evaporation and ice and binary condensation rates, respectively. Owing to the warmer temperatures than in our previous active methane simulations, binary condensation now occurs again, though only very close to the poles (poleward of ~70°), peaking in local summer and early spring. Ice condensation is also largely restricted to poleward of ~60°, where it occurs largely during late local spring/early summer. In addition, occasional clouds occur at low and mid latitudes, though these clouds (and clouds in general) are far less frequent than observed on Titan itself. Fig. 19d shows the precipitation predicted in FIN_LH_TI. All five condensation events that occur outside of high latitudes are sufficiently concentrated that they result in surface precipitation. Finally, Fig. 19e shows the surface methane distribution predicted for the higher TI value, which rapidly results in a larger hemispheric asymmetry than in our previous simulations.

6. Summary and conclusions

We have used the troposphere–stratosphere TitanWRF GCM to simulate Titan's methane cycle, investigating: (i) the impact of latent heating feedbacks ('active methane') on the circulation and methane cycle produced; (ii) the distribution of surface methane

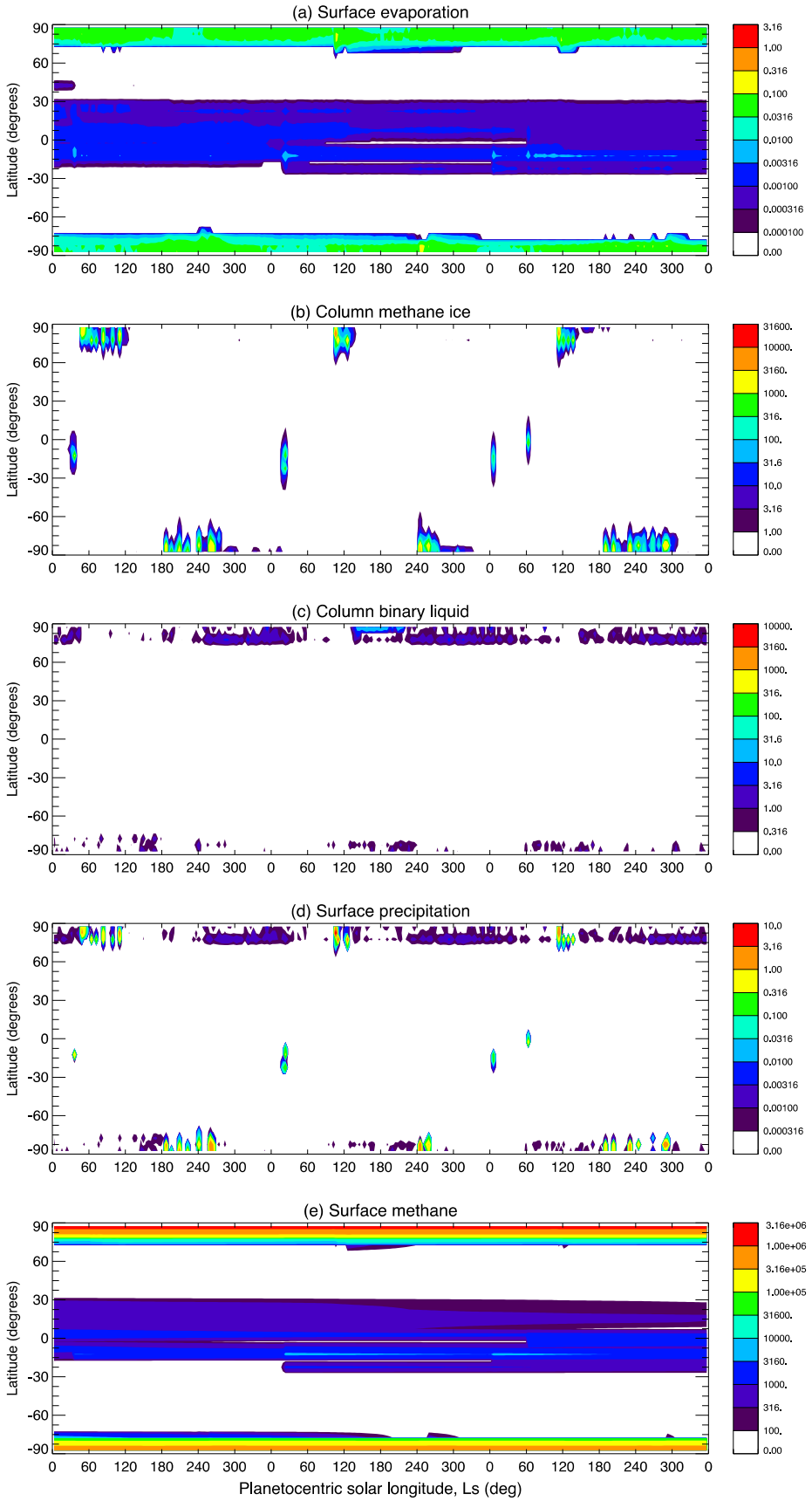

Fig. 19. Zonal mean (a) surface evaporation, (b) tropospheric column ice condensation, (c) tropospheric column binary methane condensation, (d) surface precipitation and (e) surface methane depth, as shown in Fig. 11a–e, but now for simulation FIN_LH_TI.

produced by our simulated methane cycle, including a proposed mechanism for the hemispheric asymmetry observed; and (iii) the realism of the simulated circulation and methane cycle. Sections 6.1–6.3 summarize these investigations, and we discuss future work in Section 6.4.

6.1. The passive and active methane cycle in TitanWRF

We describe 'active'/'passive' methane simulations as those with/without latent heating feedbacks. In both cases, TitanWRF's tropospheric circulation consists of high latitude polar cells in late winter through summer, and seasonally-evolving Hadley cells. The latter consists of a single cell around solstice with upwelling at summer high latitudes, and two cells the rest of the year with convergence and upwelling following the location of the Inter-Tropical Convergence Zone (ITCZ), which passes from the summer hemisphere across the equator at roughly equinox. The timing and location of atmospheric condensation and surface precipitation in TitanWRF is linked to (a) frequent strong polar upwelling during local spring and summer in the polar cells, and (b) tropospheric methane convergence and upwelling in the ITCZ, as also found in Mitchell et al. (2006), Schneider et al. (2012), and Lora et al. (2014, 2015). In simulations with methane available everywhere on the surface, clouds thus peak from mid spring to mid summer at high latitudes, and follow the locations of peak methane convergence and peak upwelling associated with the ITCZ (from summer mid/high latitudes in one hemisphere around solstice, to low latitudes around equinox, into summer mid/high latitudes in the opposite hemisphere around the following solstice). In simulations with finite surface methane, which result in a largely dry low and mid latitude surface (see Section 6.2), the circulation still transports methane from the remaining source regions (at high latitudes) to low and mid latitudes. Low and mid latitude condensation thus continues to occur, but at far lower rates, and low/mid latitude precipitation ceases altogether in passive simulations. Significant interannual variability exists in the occurrence and timing of clouds and precipitation; however, the active simulation typically produces more low latitude condensation and precipitation as the ITCZ moves from south to north across the equator from late northern winter through northern spring, versus the opposite time of year.

In active simulations the methane cycle impacts the circulation via latent cooling of the surface (and hence near-surface atmosphere) during surface methane evaporation, and latent heating/-cooling of the atmosphere during atmospheric methane condensation/evaporation. In finite surface methane simulations, surface evaporative cooling occurs only at high latitudes (since low/mid latitudes are normally dry), which reduces the spring/-summer high latitude thermal forcing and weakens the strong upwelling in the polar cells. It also produces stronger thermal gradients in the lowest ~5–10 km of the atmosphere at ~60–70° latitude and significant summer polar jets. The restriction of the latitude range of peak thermal forcing from pole-to-pole in the passive case to less than ~45° in the active case, and the sharp thermal front at higher latitudes, reduces the latitudinal extent of the solsticial Hadley cells below ~5–10 km. This is reflected in the reduced latitudinal extent of the ITCZ, which now moves between ~45°N and S (rather than nearly pole to pole in the passive case), as found in Mitchell et al. (2006). Peak vertical motion in the ITCZ and at the spring/summer pole merge in summer in the passive case but remain separate in the active case, producing a double maxima in the summer vertical motion field. TitanWRF's stratospheric circulation is also impacted by the changes to the tropospheric forcing and circulation (see Section 6.3).

The active methane cycle differs from the passive due to both thermodynamical effects and the circulation changes described above. The evaporative cooling feedback reduces the amount of methane evaporation, resulting in lower methane mmrs and less high latitude cloud and precipitation. However, 'moist' convection produces clouds that are far more extended in the vertical, as latent heat release during condensation produces stronger upwelling which triggers more condensation at higher altitudes (as methane there is lifted into cooler regions). This also has the effect of transferring heat upward, resulting in a slightly more stable temperature profile in the lower troposphere than in the passive case. Once condensation is initiated, it is more likely to condense out an entire column rather than only one layer or so, and strong moist convection events produce occasional precipitation in low and mid latitudes in active simulations (unlike passive simulations, despite the larger methane mmrs at these latitudes in the passive case). The intensity, timing and location of condensation at all latitudes in active simulations is also affected by the changes to the strength of the polar cells and the reduced latitudinal extent of the Hadley circulation and ITCZ described above.

6.2. Hemispheric asymmetry in TitanWRF's surface methane distribution

On Titan, most lakes are found poleward of ~60° in the north, with few lakes and far less area covered by them in the south, and with predominantly dry low and mid latitudes. TitanWRF simulations with 'finite' surface methane were run out to a full (atmosphere + surface) steady state – i.e., were continued until they produced roughly repeating seasonal cycles with no further long term changes in the atmospheric or surface methane distribution. These simulations show the drying of low and mid latitudes, with net transport of surface methane to high latitudes, as described in Mitchell (2008). In addition, TitanWRF predicts that more surface methane will accumulate in the north, as observed. For passive methane, significant surface methane accumulates poleward of ~75° latitude in both hemispheres, with a thicker methane reservoir in the north, while transient surface methane follows precipitation between ~65° and 75° latitude and lasts well under a year. For active methane, significant surface methane accumulates poleward of ~60° in the north and ~70° in the south, with the northern reservoir again thicker, while transient surface methane follows infrequent but intense precipitation at a wide range of other latitudes and lasts up to several years. Both thus show a north–south asymmetry in the total abundance of high latitude surface methane, though only the active simulation shows a greater surface area of permanent surface methane cover in the north.

The observed surface methane asymmetry has been attributed to the present day asymmetry in solar forcing (with perihelion at $L_s = 279°$, shortly after southern summer solstice) (e.g. Aharonson et al., 2009), analogous to the asymmetry of surface water ice on Mars (Richardson and Wilson, 2002). To test this, we performed an active simulation with perihelion shortly after northern summer solstice (at $L_s = 99°$), and confirmed that the asymmetry reversed, with a greater thickness and surface area of methane in the south. Given the very small net annual methane transport between hemispheres relative to the total amount of methane involved, which made the result potentially susceptible to very small numerical errors in the transport scheme, this 'reversed perihelion' simulation was crucial to ensure that the asymmetry was produced for the right reason and was a robust result. Schneider et al. (2012) first showed that methane accumulated preferentially in the north, but did not perform such a test; however, Lora et al. (2014) demonstrated a similar reversal to that shown here.

We suggest that the mechanism behind the hemispheric asymmetry is as follows: On average, more methane can be held in the high-latitude atmosphere during the warmer perihelion (currently southern) summer than during the cooler (currently northern)

aphelion summer. The perihelion summer is shorter; however, the non-linear relationship between temperature and saturation vapor pressure more than compensates for this. More total methane is thus available (in the summer high latitude atmosphere) for transport into the opposite, methane-depleted winter hemisphere during the summer that is close to perihelion. Over the course of many years, this mechanism results in the depletion of surface methane in the south, and the accumulation of surface methane in the north, with the reverse happening when the timing of perihelion is reversed.

This all assumes an equal area of surface methane at high latitudes in both hemispheres. However, as southern high latitude methane is lost via the above process, the amount of net surface methane loss during summer decreases, until for some surface methane asymmetry a balance is achieved between the net north–south methane transport during perihelion summer and the net south–north transport during aphelion summer. I.e., in the steady state, the reduced source area *available* for evaporation in the south compensates for the greater intensity of southern summer net evaporation, producing total transport away from southern high latitudes that exactly balances the amount transported away from the north in their respective summers, and hence no further change in the long-term surface methane distribution occurs. This is consistent with the surface methane asymmetry in our active simulations, which show a greater surface area of permanent methane cover at northern high latitudes.

Results are less conclusive for our passive simulation, which shows only an asymmetry in the total *mass* (depth) not surface area of permanent methane cover. While in reality it will affect surface thermal inertia and heat transport, in this version of TitanWRF the methane depth cannot impact evaporation rates (unless it is so shallow that surface methane is about to exhaust) so cannot play into the above mechanism. However, there is longer-lasting *transient* surface methane in northern versus southern mid-to-high latitudes, which may provide the balance in fluxes required.

The asymmetry produced by Schneider et al. (2012) involved a hypothesized surface/sub-surface transport of methane from the poles to mid latitudes, though it is unclear whether this additional transport was *required* to achieve a steady state solution. Using TitanWRF we produce a hemispheric asymmetry in surface methane without requiring such additional transport to resupply lower latitudes, although the simulated asymmetry is much smaller than observed on Titan, and surface methane covers a smaller latitude range than observed in the north. This result is consistent with the findings of Lora et al. (2015), who also include only atmospheric methane transport. It is possible that the areal extent as well as depth of surface methane would have been impacted had we initialized our finite methane simulations with a greater methane abundance. But it is more likely that a better representation of fractional surface type (e.g. ice, lake, porous regolith), topography and surface runoff, and vertical and horizontal subsurface methane transport, is needed to fully match the observed lake distribution, requiring an LSM (see Section 6.4). The approach of Schneider et al. (2012) may have been intended to approximate such a scheme, though adding an LSM permits the investigation to be conducted in a far more complete and physically consistent manner.

6.3. The realism of TitanWRF's methane cycle

Our baseline active simulation reproduces several aspects of the observed atmospheric state and methane cycle. In particular, the timing and latitudes of condensation (as a proxy for clouds) and surface precipitation are generally as observed: concentrated at the poles through a large fraction of the year, and also moving through mid and low latitudes in line with the motion of the ITCZ through the year. In detail, however, we do not reproduce the exact timing/location of all observed clouds and rainfall events, and the GCM produces too few condensation/precipitation events compared to Titan itself. In addition, we predict surface and tropospheric temperatures, and tropospheric methane mole fractions, that are significantly smaller than observed by the Huygens probe. Methane relative humidities are more consistent with observations in the lower half of the troposphere (since both temperature and methane mole fraction are smaller), but fall too rapidly in the upper half. In Section 6.4 we review the likely impact of some of the approximations and assumptions made in these simulations, and how they will be improved in future work.

TitanWRF is not only a tropospheric model but also resolves the stratosphere and lower mesosphere up to ~400 km, and was previously shown to produce good agreement with the observed large magnitudes and general pattern of stratospheric superrotation (Newman et al., 2011). We find the impact of an active methane cycle on stratospheric temperatures and winds is relatively small, though peak zonal winds are weakened by ~12%, making them slightly less realistic. However, reduced zonal wind speeds in the lower stratosphere, with a stronger gradient in wind speed above them, is more consistent with observations.

6.4. Discussion and future work

In this work we made several simplification and approximations. No detailed cloud microphysics meant that we did not model the production of cloud particles and condensation, or the interaction between the haze, ethane (solid and vapor) and methane (solid, liquid and vapor) distributions, all of which may be vital to simulating a realistic methane cycle and matching all observations. We also neglected the lowering of the freezing point temperature for binary methane clouds (with dissolved nitrogen), meaning that binary condensation was restricted below ~5 km (with ice clouds forming above this), rather than extending to ~15 km as likely occurs on Titan itself. This will have impacted the amount of condensation predicted to occur, as the saturation vapor pressure required for binary condensation at a given temperature is lower than that for pure methane ice (Eq. (1)). In addition, we calculated the binary methane saturation vapor pressure making simplifying assumptions about two coefficients, which will also have impacted our results.

We used a large scale condensation scheme to predict rates of atmospheric condensation/evaporation and latent heating/cooling, followed by a vertical diffusion scheme that mixed heat, momentum, and methane more vigorously in unstable regions. By doing so we effectively captured many of the effects of moist convection, though not to the degree and accuracy provided by including a full moist convection parameterization (which can include representations of convective overshoots, entrainment and detrainment, etc.). Several Titan GCMs use a simple version of a moist convection parameterization – a moist convective adjustment (MCA) scheme – to mimic the sub-grid scale effects of clouds and moist convection by redistributing heat and methane, relaxing the latter toward a prescribed profile on a pre-set timescale (e.g., Mitchell et al., 2006; Schneider et al., 2012). However, these are also not an ideal solution, as they require fairly *ad hoc* assumptions to be made about the most appropriate relaxation profile and timescale to use. A more complete and satisfying approach is to parameterize sub-grid scale mixing by both boundary layer eddies and moist convective cloud processes – i.e., both dry and moist convection – using an Eddy Diffusion Mass Flux (EDMF) scheme. These are increasingly common in Earth (e.g. Sušelj et al., 2012) and now also Mars (Colaïtis et al., 2013) GCMs, and provide a more physically-based representation of sub-grid scale mixing processes. We are

presently developing such a scheme for TitanWRF. As a prelude to this, we have added an MCA scheme into TitanWRF to enable comparison with other models that already employ such a scheme. The impact on results is less intense and less 'patchy' condensation and precipitation, due to the smoother relaxation of heat and methane using an MCA scheme, rather than the mixing of latent heat updates using the present (large scale condensation + vertical diffusion) schemes.

In this work we do not track surface type and assume a moisture availability of 0.5 everywhere, equivalent to assuming that surface methane is partially adsorbed into the top regolith layer, as opposed to e.g. forming a liquid lake or diffusing deeper into the sub-surface. This is a reasonable starting point, but we will explore the sensitivity to this assumption in future work as a prelude to including an LSM into TitanWRF (e.g. Chen and Dudhia, 2001). This would include sub-surface vertical and horizontal transport of methane and represent topography and surface runoff, enabling us to predict e.g. the fractional coverage of a surface grid box by different surface types (ice, lake, porous regolith, etc.), the amount of methane adsorbed into the regolith versus the amount remaining on the surface, and the vertical distribution of methane in the sub-surface. An LSM would also allow us to model the lake distribution, rather than merely the 'wetness' of the surface, permitting more direct comparison with lake observations. In Section 5 we demonstrated that greatly increasing surface thermal inertia improved the match to surface temperature observations, but also noted that it implied an overly large effective thermal conductivity. However, this demonstrated the large potential impact of surface properties on temperature and thus the methane cycle. More sensitivity studies will be performed in the future, and the LSM should permit more realistic spatial variation of such properties in future work.

More work is needed in general to improve our match to observations of Titan's tropospheric and surface temperatures. Although relative humidities are comparable to those observed in the lower troposphere (since reduced temperatures also result in smaller methane abundances) the nature of the condensate that forms is still affected, as is heat transport and the circulation overall. We already use a correlated-k radiative transfer scheme in MarsWRF (Mischna et al., 2012) and this will be implemented in TitanWRF using Cassini–Huygens-based optical properties, replacing the current version of the McKay et al. (1989) scheme, and calibrated to match observed temperature profiles. The new scheme will be run with active haze (including two-moment haze microphysics and transport) to permit feedbacks between the circulation and haze distribution, which are not included at present.

Acknowledgments

We thank Christopher McKay for providing us with his updated Titan radiative transfer scheme. This work was funded by grants from NASA's Outer Planets Research program (grant number NNX11AM35G) and the NASA Astrobiology Institute, and simulations were performed on the Pleiades cluster at the High End Computing facility at NASA Ames. We also thank Sébastien Lebonnois and one anonymous reviewer for their detailed reviews.

References

Achterberg, R.K. et al., 2008. Titan's middle-atmospheric temperatures and dynamics observed by the Cassini Composite Infrared Spectrometer. Icarus 194, 263–277. http://dx.doi.org/10.1016/j.icarus.2007.09.029.

Achterberg, R.K. et al., 2011. Temporal variations of Titan's middle-atmospheric temperatures from 2004 to 2009 observed by the Cassini/CIRS. Icarus 211, 686–698. http://dx.doi.org/10.1016/j.icarus.2010.08.009.

Aharonson, O. et al., 2009. An asymmetric distribution of lakes on Titan as a possible consequence of orbital forcing. Nat. Geosci. 2, 851–854.

Anderson, C., Samuelson, R., Achterberg, R., 2012. Titan's stratospheric condensibles at high northern latitudes during northern winter. Titan through Time III Workshop, NASA GSFC, p. 59. <http://spacescience.arc.nasa.gov/events/titan-through-time-ii-workshop>.

Barth, E.L., Toon, O.B., 2006. Methane, ethane, and mixed clouds in Titan's atmosphere: Properties derived from microphysical modeling. Icarus 182, 230–250.

Bird, M.K. et al., 2005. The vertical profile of winds on Titan. Nature 438 (8). http://dx.doi.org/10.1038/nature04060.

Bouchez, A.H., Brown, M.E., 2005. Statistics of Titan's south polar stratospheric clouds. Astrophys. J. 618, L53–L56. http://dx.doi.org/10.1086/427693.

Brown, M.E., Bouchez, A.H., Griffith, C.A., 2002. Direct detection of variable tropospheric clouds near Titan's south pole. Nature 420, 795–797.

Brown, R.H. et al., 2008. The identification of liquid ethane in Titan's Ontario Lacus. Nature 454, 607–610. http://dx.doi.org/10.1038/nature07100.

Brown, M.E., Roberts, J., Schaller, E., 2010. Clouds on Titan during the Cassini prime mission: A complete analysis of the VIMS data. Icarus 205 (2), 571–580.

Chen, F., Dudhia, J., 2001. Coupling an advanced land surface-hydrology model with the Penn State-NCAR MM5 modeling system. Part I: Model implementation and sensitivity. Mon. Weather Rev. 129, 569–585.

Colaïtis, A. et al., 2013. A thermal plume model for the martian convective boundary layer. J. Geophys. Res.: Planets 118, 1468–1487.

Cordier, D. et al., 2009. An estimate of the chemical composition of Titan's lakes. Astrophys. J. 707, L128–L131. http://dx.doi.org/10.1088/0004-637X/707/2/L128.

Cordier, D. et al., 2013. Correction to an estimate of the chemical composition of Titan's lakes. Astrophys. J. 768 (1), L23. http://dx.doi.org/10.1088/2041-8205/768/1/L23.

Cottini, V. et al., 2012. Spatial and temporal variations in Titan's surface temperatures from Cassini CIRS observations. Planet. Space Sci. 60, 62–71.

Deardorff, J.W., 1972. Parameterization of the planetary boundary layer for use in general circulation models. Mon. Weather Rev. 100, 93–106.

Fulchignoni, M. et al., 2005. In situ measurements of the physical characteristics of Titan's environment. Nature 438, 1–7.

Griffith, C.A., 2009. Storms, polar deposits and the methane cycle in Titan's atmosphere. Philos. Trans. R. Soc. A 367, 713–728.

Griffith, C.A. et al., 1998. Transient clouds in Titan's lower atmosphere. Nature 395, 575–578.

Griffith, C.A., Hall, J.L., Geballe, T.R., 2000. Detection of daily clouds on Titan. Science 290, 509–513.

Griffith, C.A. et al., 2005. The evolution of Titan's mid-latitude clouds. Science 310, 474–477. http://dx.doi.org/10.1126/science.1117702.

Griffith, C.A. et al., 2006. Evidence for a polar ethane cloud on Titan. Science 313, 1620–1622. http://dx.doi.org/10.1126/science.1128245.

Hanel, R.A. et al., 1981. Infrared observations of the saturnian system from Voyager 1. Science 212, 192–200.

Hayes, A. et al., 2008. Hydrocarbon lakes on Titan: Distribution and interaction with a porous regolith. Geophys. Res. Lett. 35, L09204. http://dx.doi.org/10.1029/2008GL033409.

Hayes, A. et al., 2011. Transient surface liquid in Titan's polar regions from Cassini. Icarus 211, 655–671. http://dx.doi.org/10.1016/j.icarus.2010.08.017.

Hong, S.-Y., Pan, H.-L., 1996. Nonlocal boundary layer vertical diffusion in a medium-range forecast model. Mon. Weather Rev. 124, 2322–2339.

Jennings, D. et al., 2009. Titan's surface brightness temperatures. Astrophys. J. 691 (2), L103–L105.

Jennings, D.E. et al., 2011. Seasonal changes in Titan's surface temperatures. Astrophys. J. 737, L15. http://dx.doi.org/10.1088/2041-8205/737/1/L15 (3pp.).

Kossacki, K.J., Lorenz, R.D., 1996. Hiding Titan's ocean: Densification and hydrocarbon storage in an icy regolith. Planet. Space Sci. 44, 1029–1037.

Kouvaris, L.C., Flasar, F.M., 1991. Phase equilibrium of methane and nitrogen at low temperatures—Application to Titan. Icarus 91, 112–124.

Kuiper, G.P., 1944. Titan: A satellite with an atmosphere. Astrophys. J. 100, 378–383.

Lellouch, E. et al., 1989. Titan's atmosphere and hypothesized ocean—A reanalysis of the Voyager 1 radio-occultation and IRIS 7.7-micron data. Icarus 79, 328–349.

Lora, J.M. et al., 2011. Insolation in Titan's troposphere. Icarus 216, 116–119. http://dx.doi.org/10.1016/j.icarus.2011.08.017.

Lora, J.M. et al., 2014. Simulations of Titan's paleoclimate. Icarus 243, 264–273. http://dx.doi.org/10.1016/j.icarus.2014.08.042.

Lora, J.M., Lunine, J.I., Russell, J.L., 2015. GCM simulations of Titan's middle and lower atmosphere and comparison to observations. Icarus 250, 516–528. http://dx.doi.org/10.1016/j.icarus.2014.12.030.

Lorenz, R.D. et al., 2008. Titan's inventory of organic surface materials. Geophys. Res. Lett. 35, L02206. http://dx.doi.org/10.1029/2007GL032118.

Lorenz, R.D. et al., 2013. A global topographic map of Titan. Icarus 225 (1), 367–377.

Luz, D., Hourdin, F., 2003. Latitudinal transport by barotropic waves in Titan's stratosphere. I. General properties from a horizontal shallow-water model. Icarus 166, 328–342.

Luz, D. et al., 2003. Latitudinal transport by barotropic waves in Titan's stratosphere. II. Results from a coupled dynamics–microphysics–photochemistry GCM. Icarus 166, 343–358.

McKay, C.P., Pollack, J.B., Courtin, R., 1989. The thermal structure of Titan's atmosphere. Icarus 80, 23–53.

Mischna, M.A., Lee, C., Richardson, M.I., 2012. Development of a fast, accurate radiative transfer model for the martian atmosphere, past and present. J. Geophys. Res. 117, E10009. http://dx.doi.org/10.1029/2012JE004110.

Mitchell, J.L., 2008. The drying of Titan's dunes: Titan's methane hydrology and its impact on atmospheric circulation. J. Geophys. Res.: Planets 113, E12. http://dx.doi.org/10.1029/2007JE003017.
Mitchell, J.L. et al., 2006. The dynamics behind Titan's methane clouds. Proc. Natl. Acad. Sci. U.S.A. 103 (49), 18421–18426.
Mitchell, J.L. et al., 2009. The impact of methane thermodynamics on seasonal convection and circulation in a model Titan atmosphere. Icarus 203, 250–264.
Mitchell, J.L. et al., 2011. Locally enhanced precipitation organized by planetary-scale waves on Titan. Nat. Geosci. http://dx.doi.org/10.1038/NGEO1219.
Montmessin, F. et al., 2007. On the origin of perennial water ice at the south pole of Mars: A precession-controlled mechanism? J. Geophys. Res. 112, E08S17. http://dx.doi.org/10.1029/2007JE002902.
Moses, J.I., Allen, M., Yung, Y.L., 1992. Hydrocarbon nucleation and aerosol formation in Neptune's atmosphere. Icarus 99, 318–346.
Newman, C.E. et al., 2011. Stratospheric superrotation in the TitanWRF model. Icarus 213 (2), 636–654.
Niemann, H.B. et al., 2005. The abundances of constituents of Titan's atmosphere from the GCMS instrument on the Huygens probe. Nature 438, 779–784. http://dx.doi.org/10.1038/nature04122.
Rannou, P. et al., 2004. A coupled dynamics–microphysics model of Titan's atmosphere. Icarus 170, 443–462.
Richardson, M.I., Wilson, R.J., 2002. Investigation of the nature and stability of the martian seasonal water cycle with a general circulation model. J. Geophys. Res.: Planets 107. http://dx.doi.org/10.1029/2001JE001536.
Richardson, M.I., Toigo, A.D., Newman, C.E., 2007. PlanetWRF: A general purpose, local to global numerical model for planetary atmospheric and climate dynamics. J. Geophys. Res.: Planets 112, E09001. http://dx.doi.org/10.1029/2006JE002825.
Rodriguez, S. et al., 2009. Global circulation as the main source of cloud activity on Titan. Nature 459, 678–682.
Rodriguez, S. et al., 2011. Titan's cloud seasonal activity from winter to spring with Cassini/VIMS. Icarus 216, 89–110.
Roe, H.G. et al., 2002. NOTE: Titan's atmosphere in late southern spring observed with adaptive optics on the W.M. Keck II 10-meter telescope. Icarus 157, 254–258.
Roe, H.G. et al., 2005. Discovery of temperate latitude clouds on Titan. Astrophys. J. 618, L49–L52. http://dx.doi.org/10.1086/427499.
Schaller, E.L. et al., 2006a. A large cloud outburst at Titan's south pole. Icarus 182, 224–229.
Schaller, E.L. et al., 2006b. Dissipation of Titan's south polar clouds. Icarus 184, 517–523. http://dx.doi.org/10.1016/j.icarus.2006.05.025.
Schaller, E.L. et al., 2009. Storms in the tropics of Titan. Nature 460 (7257), 873–875.
Schneider, T. et al., 2012. Polar methane accumulation and rainstorms on Titan from simulations of the methane cycle. Nature. http://dx.doi.org/10.1038/nature10666, 481, 58-61.
Skamarock, W.C. et al., 2005. A Description of the Advanced Research WRF Version 2: NCAR Technical Note.
Sotin, C. et al., 2012. Observations of Titan's northern lakes at 5 μm: Implications for the organic cycle and geology. Icarus 221, 768–786.
Stofan, E.R. et al., 2007. The lakes of Titan. Nature 445, 61–64.
Sušelj, K., Teixeira, J., Matheou, G., 2012. Eddy diffusivity/mass flux and shallow cumulus boundary layer: An updraft PDF multiple mass flux scheme. J. Atmos. Sci. 69, 1513–1533.
Thompson, W.R., Zollweg, J.A., Gabis, D.H., 1992. Vapor–liquid equilibrium thermodynamics of N_2 + CH_4: Model and Titan applications. Icarus 97, 187–199.
Tokano, T., 2005. Meteorological assessment of the surface temperatures on Titan: Constraints on the surface type. Icarus 173, 222–242.
Tokano, T. et al., 2001. Simulation of Titan's atmospheric methane cycle by a general circulation and the effect of supersaturation of methane on the atmospheric circulation. Icarus 153, 130–147.
Tomasko, M.G. et al., 2005. Rain, winds and haze during the Huygens probe's descent to Titan's surface. Nature 438, 765–778. http://dx.doi.org/10.1038/nature04126.
Turtle, E.P. et al., 2009. Cassini imaging of Titan's high-latitude lakes, clouds, and south-polar surface changes. Geophys. Res. Lett. 36, L02204. http://dx.doi.org/10.1029/2008GL036186.
Turtle, E.P. et al., 2011a. Seasonal changes in Titan's meteorology. Geophys. Res. Lett. 38, L03203. http://dx.doi.org/10.1029/2010GL046266.
Turtle, E.P. et al., 2011b. Shoreline retreat at Titan's Ontario Lacus and Arrakis Planitia from Cassini Imaging Science Subsystem observations. Icarus 212, 957–959. http://dx.doi.org/10.1016/j.icarus.2011.02.005.
Turtle, E.P. et al., 2011c. Rapid and extensive surface changes near Titan's equator: Evidence of April showers. Science 331, 1414. http://dx.doi.org/10.1126/science.1201063.
Tyler, G.L. et al., 1981. Radio science investigations of the Saturn system with Voyager 1 – Preliminary results. Science 212, 201–206.
Zebker, H. et al., 2014. Surface of Ligeia Mare, Titan, from Cassini altimeter and radiometer analysis. Geophys. Res. Lett. 41, 308–313. http://dx.doi.org/10.1002/2013GL058877.